January 1971

NASA CR-116513

Progress Report to the National Aeronautics & Space Administration, on Grant NGL-40-002-080 (Plasticity Aspects of Fracture Mechanics Analysis)*:

Progress Report on Elastic-Plastic Finite Element Analysis of Cracked Solids

Introductory Note: Several topics relating to plasticity aspects of fracture are under study through Grant NGL-40-002-080. This report deals exclusively with one phase of the work, namely elastic-plastic finite element analysis. It reports progress and problems to date on studies directed toward: 1) the analysis of practical fracture test specimens, especially the notched round tensile bar employed in the experimental program, and 2) the development of versatile singularity elements for crack tips, of a form which are readily merged with standard elements of an isoparametric or triangular type. Unanticipated difficulties have arisen in attempts at obtaining the highly accurate numerical solutions which have been a goal of the study. These are explained here together with a presentation of numerical results. The work has been carried out by Mr. D. M. Tracey, Research Assistant on Grant NGL-40-002-080.

Introduction

The numerical analysis of cracked solids under external load is difficult because of the singular deformation state near a crack tip. Elastic crack solutions are governed by an inverse square root stress and strain singularity [1] while elastic perfectly-plastic solutions for stationary cracks involve a $1/r$ shear strain crack tip singularity [2]. Hutchinson [3] and Rice and Rosengren [4] have found near tip solutions to power law hardening materials which have stresses and strains exhibiting $N/(1+N)$ and $1/(1+N)$ types of singularity respectively, where N is the hardening exponent. Rice [2] has offered the Prandtl slipline stress field as the asymptotic stress distribution at the tip of a sharp crack in a non-hardening material in plane strain.

The goal in the present work is to obtain finite element solutions to typical

* Held by Brown University, Division of Engineering, with Professors C. Mylonas and J. R. Rice as principal investigators.

elastic-plastic problems which are reliable at the troublesome singularity as well as being accurate globally. A solution to the circumferentially grooved round tensile bar is described in this progress report. The numerical treatment of the near tip region was based on the method used by Levy et al. [5] in their study of the small scale yielding boundary layer problem. They developed the "polar" element, a four-node element whose edges are described by lines at constant angle and arcs of constant radius in a polar coordinate system (r,θ). Centering the coordinate system at the crack tip and choosing an (r,θ) bilinear interpolation function allows a $1/r$ strain variation within the element. Using this they obtained a stress solution very close to the Prandtl field.

The geometry of the round bar motivated the use of straight edged isoparametric elements which when focused into the crack tip allows the $1/r$ strain variation. Surprisingly this procedure failed to give a reasonable near tip solution. The small scale yield solution to this round bar problem differed significantly from Levy et al. The asymptotic boundary layer problem was then used as a test problem to learn the essential differences between the polar and focused isoparametric elements. It is concluded that two features of these singular elements require further study: First is the use of the area average stress as an approximation to the stress state at each of the integration stations of the element, and second is the singular dilatation allowed by the interpolation function. Currently a new element is being developed which will allow only a singular shear strain in its set of admissible deformations.

The large scale yielding solution to the round bar problem demonstrated that the numerical method of calculating the elastic-plastic stress strain matrix that is in common use (Marcal and King [6]) is a source of accumulative error. Stated briefly this method bases the plastic flow rule for an increment on the initial stress state, instead of on some estimated average stress state experienced during the increment, with the result that the stress state wanders away from the yield surface. Currently a revised procedure is being adopted to correct this problem.

Numerical Procedure

The finite element procedure used consisted of transforming the actual elastic-plastic problem into that of solving a system of linear algebraic equations in the

displacements (displacement increments for plasticity) of a finite number of "nodes" of the body. The coefficient matrix of this system is constructed from the stiffness matrices of "elements" of material associated with the nodes. The behavior within the elements is a priori specified in terms of the unknown nodal motion through the elements' interpolation functions. The element stiffness matrix depends exclusively on the interpolation function chosen and the constitutive law of the material.

If $\underset{\sim}{\beta}(X)$ is the matrix derived from the interpolation function which relates an element's nodal displacement increments, $\Delta\underset{\sim}{\delta}$, to strain increments at an interior point X, $\Delta\underset{\sim}{\varepsilon}(X)$, and $\underset{\sim}{D}$ is the incremental stress-strain matrix, the element stiffness is written as

$$\underset{\sim}{K} = \int_A \underset{\sim}{\beta}^T \underset{\sim}{D}\, \underset{\sim}{\beta}\, dA \tag{1}$$

For a Prandtl-Reuss material that continues to load $\underset{\sim}{D}$ depends upon the elastic coefficients $\underset{\sim}{D}^{el}$, the current work-hardening rate $H'(\bar{\varepsilon}_p)$, and the stress state; the dependence on the latter is through the vector

$$\partial\bar{\sigma}/\partial\underset{\sim}{\sigma} = 3\left[S_1, S_2, \cdots\right]/2\sigma_o$$

where S_i are the deviatoric stresses and σ_o the current yield stress. The matrix expression for $\underset{\sim}{D}$ is

$$\underset{\sim}{D} = \underset{\sim}{D}^{el.}\left(\underset{\sim}{I} - \frac{(\partial\bar{\sigma}/\partial\underset{\sim}{\sigma})^T\, \partial\bar{\sigma}/\partial\underset{\sim}{\sigma}\, \underset{\sim}{D}^{el.}}{H' + \partial\bar{\sigma}/\partial\underset{\sim}{\sigma}\, \underset{\sim}{D}^{el.}\, (\partial\bar{\sigma}/\partial\underset{\sim}{\sigma})^T}\right) \tag{2}$$

$\underset{\sim}{I}$ is the identity matrix.

Integration of eq. (1) is usually done by some quadrature rule that approximates the integral as the sum of products of the integrand evaluated at selected stations X_N times an associated fraction or "weight" of the total area. The sum of the weights equals the total area.

The algorithm of an elastic-plastic solution begins with the assembly of the master stiffness matrix from the element stiffnesses obtained using $\underset{\sim}{D}^{el}$ in

eq. (1). The equations are solved, stresses are evaluated at selected position(s) within the elements, and the solution is then scaled to render that stress state with the greatest equivalent shear to the point of incipient yield. Next a "small" load increment is specified, the meaning of "small" will be explained shortly. Each stress state in the mesh is checked to see if during the load increment the region would yield if the deformation continues proportionate to the previous solution. For those regions that would yield, a weighted average $\underset{\sim}{D}$ matrix is constructed from $\underset{\sim}{D}^{e\ell}$ and $\underset{\sim}{D}^{e\ell-p\ell}$ according to the method of Marcal and King [6]. For the points at yield $\underset{\sim}{D}^{e\ell-p\ell}$ is formed based on the current stress state. With the new master stiffness matrix a displacement increment solution is obtained, the stress increments are added to the previous stress states and the process repeats itself until the final load has been achieved. Since the dependence of the constitutive matrix on the stress state is the feature that makes this a non-linear problem, the size of the load increment must be judged according to the size of stress increment it produces. Since for perfectly plastic materials continuing to load the only permissible stress increment is tangent to the yield surface there is always an amount of error involved in using finite load increments. The permissible size of a load increment depends upon the tolerance set for the amount a stress increment can venture away from the yield surface.

The near tip elements used in the present study were given interpolation functions which allow the expected singular deformation. The $1/r$ shear singularity expected in the plastic case motivated the use of centered trapezoidal shaped isoparametric elements, fig. 1. The elements nearest the crack tip have two coincident nodes at the tip. This allows the displacement discontinuity ar $r = 0$ that is associated with a $1/r$ singularity. The isoparametric interpolation function is expressed in terms of the element's natural coordinates (ξ,η) as

$$\underset{\sim}{u} = \underset{\sim}{b}_1 + \underset{\sim}{b}_2 \xi + \underset{\sim}{b}_3 \xi\eta + \underset{\sim}{b}_4 \eta \qquad (3)$$

The cartesian displacement vector $\underset{\sim}{u}(X)$ depends upon the nodal displacement vectors which are linearly related to the generalized displacements $\underset{\sim}{b}_i$. For the trapezoids of fig. 1 which are considered in the unit square $(0 \leq \xi \leq 1,\ 0 \leq \eta \leq 1)$ in parameter space the natural coordinates are

$$\left.\begin{aligned} \xi &= s/s^* \\ \eta &= (\tan\psi/\tan\alpha + 1)/2 \end{aligned}\right\} \qquad (4)$$

The strain distribution in this element referred to the local coordinate system (s,t) is

$$\begin{aligned} 2\epsilon_{ss} &= (U_J - U_I)\cot\alpha\,(\tan\psi/s) + \text{const} \\ 2\epsilon_{tt} &= (V_I - V_J)\cot\alpha\,(1/s) + \text{const} \\ 2\gamma_{st} &= (U_I - U_J)\cot\alpha\,(1/s) + (V_J - V_I)\cot\alpha\,(\tan\psi/s) \\ &\quad + \text{const} \end{aligned} \qquad (5)$$

The constants depend upon the displacements of nodes I,J,K,L and the element dimensions. Clearly the $1/s$ terms indicate the element is capable of duplicating the $1/r$ singularity characteristic of the non-hardening case.

The inverse square root elastic singularity motivated the design of an element with the shape of those in fig. 1 with the interpolation function

$$\underline{u}(x) = \underline{b}_1 + \underline{b}_2\sqrt{\xi} + \underline{b}_3\sqrt{\xi}\,\eta \qquad (6)$$

The coincident nodes of the near tip elements are constrained to move together in this formulation. This elastic singularity element has been used to obtain very accurate stress intensity factors in typical elastic crack problems [7]. An interpolation function that provides a strain distribution with $1/r$ and $1/\sqrt{r}$ terms is

$$\underline{u}(x) = \underline{b}_1 + \underline{b}_2\sqrt{\xi} + \underline{b}_3\sqrt{\xi}\,\eta + \underline{b}_4\eta \qquad (7)$$

There remain questions to be considered such as whether or not an exact elastic interpolation function should be used to gain the elastic solution to a body which actually experiences yielding under infinitesimal load. There is also the problem of determining the most rigorous method of numerical integration of the element stiffness matrix. The questions of how many quadrature stations are necessary and what stress states within an element should be stored are the basis of the problem. It is found that the solution is quite sensitive to all of these choices, a detailed discussion of these points appears in the last section.

Circumferentially Cracked Round Bar

The first problem solved was the circumferentially cracked round bar with an inside to outside diameter ratio (d/D) of 1/2 . The length was chosen as 3.75 D which was sufficient to obtain a uniform stress solution at the end when a uniform axial displacement was imposed there. A mesh with 768 degrees of freedom associated with 340 axisymmetric ring elements was employed in the upper half of the body which is naturally described in terms of a (ρ,z,ϕ) cylindrical coordinate system. The centerline is along the z axis and the crack is along the line $(d/2 \leq \rho \leq D/2,0)$ in a meridional plane ϕ = const , fig. 2. When viewed in the ρ - z plane the cross sections of the elements were centered trapezoids near the tip, rectangles near the end, and arbitrary quadrilaterals elsewhere. There were 300 trapezoids in 13 rings centered about the crack tip. These elements had an angular dimension of $\pi/24$. The nodes described arcs of radius

$$r = [0, 1, 1.5^2, 2^2, 2.5^2, \cdots, 6^2, 45.4, 59.2]\, d/72 \qquad (8)$$

The integration of the element stiffnesses was accomplished by a 9 point Gaussian quadrature. The integration stations within a near tip element using this procedure are pictured in fig. 3d. When viewed in (ξ,η) parameter space the stations are at the intersections of the coordinates lines $(1 \pm \sqrt{3/5})/2$ and 1/2 . The weight of the ξ-η area associated with the "corner" stations is 25/324 , the center weight is 16/81 and the other stations on the coordinate lines ξ,η = 1/2 have weight 10/81 .

In the integration a further approximation was made. Only the stress state of the center of the element was stored. If this state satisfied yield the $\underset{\sim}{D}$ matrix for all integration stations was derived based on this state. This approximation was made with the inkling that stress gradients within a plastic element are not large enough to provide a significant variation of the $\underset{\sim}{D}$ matrix within the element. Subsequent findings that the numerical procedure of the early deformation history near the crack tip has a marked influence on the large deformation results there renders questionable the effect this approximation has in view of its obvious inadequacy when the element is along the elastic-plastic boundary.

Two elastic, incipient yield solutions were obtained. The first was gained by using the isoparametric interpolation function for all elements, the second formu-

lation made use of the "dual" singularity interpolation function (7) for the near tip elements. Plots of the inplane stress components at the near tip element centers appear in figs. (4a,b,c) for these solutions along with the stress distribution of the leading term of the Williams expansion for plane strain with

$$K/(2\pi r)^{1/2} = 1.07\ \sigma_o \qquad (9)$$

which is satisfied when one point at radius r is at yield. For the geometry considered, Bueckner [14] gives the stress intensity factor as

$$K = 2.46\ \sigma_\infty \sqrt{d} \quad \pm 1\% \qquad (10)$$

Eqs. (9) and (10) taken together predict yield at the near tip element midpoint, $r/d = 1/144$, when

$$\sigma_\infty / \sigma_o = 0.093 \qquad (11)$$

The isoparametric solution had $\sigma_\infty/\sigma_o = 0.108$ while the dual singularity solution predicted $\sigma_\infty/\sigma_o = 0.0916$ at incipient yield.

At the near tip element centers the circumferential strain was of the same order of magnitude as the in-plane normal strains. This suggests that the state of plane strain that exists at the crack tip is very localized, prevailing in a region less than $r/d = 1/144$ about the tip.

The dual singularity solution was chosen as the best and further loading was continued from this solution; although the isoparametric interpolation function was used thereafter (once yielding takes place there is no reason to expect any singularity other than the $1/r$ form). The displacement of the end of the bar was increased to a value of 15.25 times the end displacement at first yield in 47 increments in the following order

7	increments of	0.25	u_o^∞
20	"	0.15	"
11	"	0.25	"
9	"	0.75	"

The load-deflection curve is presented in fig. 5. The curve levels off at $\sigma_{net} = 2.72\ \sigma_o$. This compares favorably with the limit pressure of axisymmetric indentation of a semi-infinite rigid perfectly plastic Tresca material given by Shield [8]. He computed the average pressure as 5.69 k where k is the flow stress in shear. The ratio of the finite element limit net stress to Shield's using the appropriate tensile yield stresses is 2.72/2.85 = 0.96. When matched in shear the ratio is 4.71/5.69 = 0.83. An important feature of the present solution is that the yield zone spreads to include the entire bar cross-section at limit load. The 2 to 1 diameter ratio chosen is seemingly too small to affect the localized flow at limit load found by Shield. The deformation was confined to a radius of 1.58 times the punch radius in Shield's solution. Fig. 6 presents the elastic-plastic boundary at progressive stages of loading. The net section stress distribution at limit load is compared to Shield's and the axisymmetric punch finite element results of Lee and Kobayashi [9] in fig. 7. The latter authors considered a specimen with geometry $D/d = 2.7$ and $L/d = 1.7$ and used a somewhat coarser mesh than the present study. Their net section distribution agrees reasonably well with the present result except near the crack tip. Shield's distribution is different in that the greatest tension is at the centerline. The present use of the Mises yield criterion makes a pointwise comparison of this Tresca solution dubious. The high stress predicted at the crack tip in the current solution is the first symptom of numerical procedural problems at the singularity, this topic will be considered shortly.

The flank opening, fig. 8, is seen to change from a small fraction of the end extension to the point where the flank opening velocity is 80% of the imposed end velocity. Of course, if the flank was included in the rigid region the limiting flank opening velocity would be 100% of the end velocity.

The near tip stresses are plotted in figs. (9a,b,c) at $\sigma_{net}/\sigma_o = 1.12$, 1.90, and 2.72 along with the Prandtl stress distribution. For the first two load states there is good agreement with the Prandtl field for σ_{zz} in the range $0 \leq \theta \leq \pi/2$. The $\sigma_{\rho\rho}$ curves are close for the first two states while the finite element $\tau_{\rho z}$ curves are much different than the Prandtl field. The $\tau_{\rho z}$ distribution for $\sigma_{net}/\sigma_o = 1.12$, 1.90 looks much like the elastic distribution, fig. 4c, for the range $0 \leq \theta \leq \pi/2$. The large almost constant shear state over the range $\theta > \pi/2$ is a clear indication that the solution is amiss in view of the traction free crack surface boundary condition. It was suspected that the size of the first plastic increments were the source of the strange stress

solution. The problem was rerun up to $\sigma_{net}/\sigma_o = 1.12$ in increments of $0.10\ u_o^\infty$ with essentially the same near tip distribution resulting. Previous finite element work has been done by Levy et al. [5] using the procedure of embedding the expected $1/r$ singularity. The solution obtained agreed very well with the Prandtl field at the crack tip. The essential difference in that work from the present is the use of an r-θ polar element instead of the centered trapezoids. Although they used a nine point integration procedure with only the midpoint stress stored like the present formulation, it has been subsequently discovered that the final near tip solution is very sensitive to the integration procedure used for straight-edged trapezoidal elements. This topic has been investigated in detail and rules have been established which define the best integration procedure to use for non-hardening plasticity. This is one of the subjects of the next section.

The finite element method calculates velocities from which strain rates are obtained. Using the constitutive matrix stress rates are obtained from the strain rates. The normality flow rule of plasticity which is incorporated in the constitutive matrix renders the stress rates tangent to the yield surface at the position of the previous stress state. While this is the correct method for infinitesimal steps, the finite load increments used may produce tangent stress increments so large that the yield condition is drastically violated. The stresses at the load $\sigma_{net}/\sigma_o = 2.72$ are unbelievably large just because of this problem. Fig. 10 is a plot of $\bar{\sigma}/\sigma_o$ for the near tip elements at $\sigma_{net}/\sigma_o = 2.72$. Obviously for the perfectly plastic material considered here this ratio should not exceed unity. In the last section a new method is formulated which uses the initial and anticipated final stress states to define a more appropriate flow rule for finite increments.

The strength of the $1/r$ shear strain singularity is defined as

$$R(\theta) = 1/\gamma_o \lim_{r \to 0} r\gamma_{r\theta} = \left[\partial u_r(0,\theta)/\partial\theta - u_\theta(0,\theta)\right]/\gamma_o \qquad (12)$$

where γ_o is the yield strain in shear $(\sigma_o/\sqrt{3}G)$. The numerical analogue for an element in the angular range $\theta_1 \leq \theta \leq \theta_2$ is

$$R(\theta_1 \text{ to } \theta_2) = \left[\frac{u_r(0,\theta_2) - u_r(0,\theta_1)}{\theta_2 - \theta_1} - \frac{u_\theta(0,\theta_2) + u_\theta(0,\theta_1)}{2}\right]/\gamma_o \qquad (13)$$

Fig. 11 is a plot of $R(\theta)/(K/\sigma_o)^2$ obtained from (13) for $\sigma_{net}/\sigma_o = 1.12$ along with the result of Levy et al. [5] and the analytical predictions [3,4,10] based on the "total strain" or "deformation" theory. The present result differs significantly from the other estimates which isn't surprising in view of the peculiar stress solution of fig. 9. The crack opening displacement can be obtained from the $R(\theta)$ function by the relation [2]

$$\delta_t = \gamma_o \int_{\pi/4}^{3\pi/4} R(\theta) \sin\theta \, d\theta$$

Levy et al. predicted that δ_t depends upon $K^2/E\sigma_o$ in small scale yielding through the relation $\delta_t/(K^2/E\sigma_o) = 0.425$. Rice [2] offered a factor of 0.613 while the non-hardening limit of the power law hardening singularity gives a value of 0.717 , [10]. The smaller amplitude of $R(\theta)$ in the present result suggests a correspondingly smaller δ_t . The plot of δ_t/d vs. $K^2/E\sigma_o d$, fig. 12, obtained from the $u_z(0,\pi)$ nodal point displacement data indeed indicates a smaller factor of proportionality between δ_t and $K^2/E\sigma_o$. The first four increments indicate a factor of 0.27 while a line through the data points of increments 7 to 13 has a slope equal to 0.34. Nevertheless, the inaccurate near tip stress distribution casts doubt on these numerical values.

The vertical displacements of the nodes on the crack face are plotted in fig. 13 for various load levels. The interesting feature of the curves is the large variation of $u_z(r,\pi)$ close to the crack tip and the nearly uniform distribution for $r/a > 1/6$. The large gradients near the tip become more pronounced with increasing load.

Asymptotic B. C. Problem

A convenient approach to studying the "small-scale yielding" of a cracked body is to use the boundary layer formulation proposed by Rice [2]. Here the crack tip deformation is investigated by enlarging the near tip region so that the characteristic elastic singularity

$$\sigma_{ij} = K/\sqrt{2\pi r}\ f_{ij}(\theta) \tag{14a}$$

$$u_i = K\sqrt{r/2\pi}/2G\ g_i(\theta) \tag{14b}$$

is approached as $r \to \infty$. This is the problem that was solved by Levy et al. [5] by using the polar element. Hence this was chosen as the problem to test the effect of the choice of numerical integration scheme and interpolation function on the near tip solution in centered trapezoidal elements.

The finite element adaptation of this formulation considered a circular region about the crack tip cut out of the enlarged region and boundary conditions applied to the outer surface according to the formula (14b) evaluated there. The near tip element dimensions are chosen sufficiently small that the stress state near the outer boundary would continue to conform to (14) even after near tip elements have yielded.

There were two meshes used. The first consisted of 10 rings of 15° elements with nodes at radii of

$$r = [0, 1, 1.5^2, 2^2, \cdots, 5.5^2]$$

Call this mesh I and the mesh consisting of 4 rings of 7.5° elements followed by 8 rings of 15° elements mesh II, fig. 14. The nodes of the latter fall on arcs of radius

$$r = [0, 0.5, 1, 1.625, 1.5^2, 2^2, \cdots 5.5^2]$$

The nodes on $r = 2.25$ not common to the adjacent 7.5° and 15° elements were constrained to move in a compatible manner [11]. Mesh I had 120 elements and 143 nodes while mesh II had 192 elements and 229 nodes. The boundary conditions at the outer surface were imposed displacements according to eq. (14b). The plastic incremental solution was gained by a continual increase in K. The loading was not continued beyond the point when the maximum extent of the plastic zone exceeded 15% of the outer radius so that the asymptotic boundary condition was at all times reasonable. The first study involved the variation of the number and

location of integration stations used in the numerical integration of the near tip element stiffness. The isoparametric interpolation function was used throughout and as in the round bar problem at each station the midpoint stress state was used to evaluate $\underset{\sim}{D}$. The stations of the four integration schemes used are pictured in fig. 3. Procedure A involved one station at the element midpoint; procedure B had three stations along $s/s^* = 1/2$ at $\tan\psi/\tan\alpha = 2/3,\ 0,\ -2/3$; procedure C had three stations along $\psi = 0$ at s/s^* 1/6, 1/2, 5/6 . Procedure D was the 9 point Gaussian quadrature rule used in the round bar problem.

The elastic near tip solutions are compared with the exact incipient yield solution in figs. 15. Solutions C and D are very close as are A and B. The former solutions have the shape of the exact elastic solution while the latter have a shape reminiscent of the Prandtl stress field. The prime ingredient which seems to couple C with D and A with B is the fact that the former two have stations at three distances along the s axis while the latter solutions have all stations at a fixed value of s .

The plastic stress solutions are compared in figs. 16. The runs A and B were continued up to $K/K_o = 4.0$ while C and D were stopped at $K/K_o = 2.2$. A and B agree reasonably well with the Prandtl solution, the deviation is greatest over the range $\theta > 3\pi/4$ where elasticity prevails. At $K/K_o = 4.0$ A remains closer to the Prandtl field than B which has σ_{xx} and σ_{yy} larger than expected in the range $\theta < \pi/4$. C and D deviate considerably from Prandtl at $K/K_o = 2.2$ in the same manner as the round bar near tip solution. It is noteworthy that the plastic shear stress distribution in each case has the same shape as its elastic counterpart. This is evidence that the elastic stress solution dictates the plastic stress solution. The effect is probably enhanced near the tip where at incipient yield many of the elastic elements are very close to yield.

Fig. 17 presents the shear singularity strength as a function of θ for procedures A and B at $K/K_o = 4.0$. A has an unrealistic valley at $\theta = 82.5°$ but the distribution obtained from smoothing this erratic behavior agrees well with the other predictions [3,4,5,10]. Ostergren [12] obtained an $R(\theta)$ with the same erratic behavior when he used a one-point (midpoint) integration rule with the polar element. Levy [13] seemed to offer a method of correcting this behavior by using a nine-point rule. This rule specified integration stations at the midpoints of 9 equally sized polar rectangles. The weight associated

with each station was the area of the corresponding region. The nine-point Gaussian rule used in procedure D failed to give a solution close to the one-point rule solution, procedure A. Procedure B has a smooth $R(\theta)$, fig. 17, however the amplitude is much smaller than the other estimates.

Some conclusions can be drawn from the preceding four solutions: Since there can be significant differences in solutions obtained by using procedures involving different approximations to the $\underset{\sim}{D}$ matrix at the integration stations, it is necessary to store the stress state at each integration station. This will allow the large stress gradients found when the element is at the elastic-plastic boundary and will be consistent with the large gradients of the $\underset{\sim}{\beta}$ matrix which are built into the element stiffness when integrations stations at different values of s are used.

The solutions of procedures A and B differed in two respects. B predicted excessive normal stresses σ_{xx}, σ_{yy} in the range $\theta < 45°$ and a much smaller shear strain singularity than that of A which, although erratic, was of the expected amplitude. A look at the $\underset{\sim}{\beta}$ matrix of the isoparametric centered trapezoidal element provides likely reasons for the differences. Eqs. (5), which are the result of the matrix multiplication $\underset{\sim}{\beta} \cdot \underset{\sim}{\delta}$, show that the dilatational strain has a singularity of the form

$$\Sigma \epsilon_{KK} \rightarrow \left\{ (U_J - U_I) \tan\psi + (V_I - V_J) \right\} \cot N\alpha / S \qquad (15)$$

Only the shear strain $\gamma_{r\theta}$ is expected to be singular in perfect plasticity [2]. This possibility is included in eqs. (5) as can be seen by the strain component γ_{st} which is equal to $\gamma_{r\theta}$ at $\psi = 0$. The source of the dilatational singularity is due entirely to the component $\epsilon_{\theta\theta}$. Procedures A and B embed the singular strain matrix $\underset{\sim}{\beta}$ into the stiffness matrix in substantially different ways. The single integration station of A is on $\psi = 0$. This integration scheme produces an element stiffness of a material with a dilatational singularity of the form

$$\Sigma \epsilon_{KK} \rightarrow (V_I - V_J) \cot N\alpha / S \qquad (16)$$

The dilatation is bounded if the solution finds V_I equal to V_J. Procedure B produces a stiffness with the singularity (15) embedded due to the integration stations at $\tan\psi/\tan\alpha = 0, \pm 2/3$. Although the strains were calculated from the solution on $\psi = 0$ so that a bounded dilatation appears from the solution if $V_I = V_J$, a singular ε_{KK} was integrated into the stiffness. It seems the use of eq. (15) in constructing the stiffness induced a solution involving both types of singularity evidenced by the excessive normal stresses and small shear singularity. If a bounded dilatation is expected, it seems reasonable to conclude from these results that integration stations should be chosen so that this is at least allowed.

Another procedure tested involved four integrations stations at the intersections of $s/s^* = 1/4, 3/4$ and $\tan\psi/\tan\alpha = \pm 1/2$. Each station is in the center of one of the four equal size subregions of the transformed $\xi - \eta$ element. The areas of the subregions were used as the weights. The stress state at each station was evaluated and stored after each load increment for use in evaluating the $\underset{\sim}{D}$ matrix there. This run was made to test the significance of the odd dependence of $\underset{\sim}{\beta}$ on ψ about the line $\psi = 0$ and also to check the constant $\underset{\sim}{D}$ assumption made previously. Mesh I was used and K was increased to $4.15\ K_o$ in six increments of $0.3\ K_o$ and three increments of $0.45\ K_o$.

The shear strain singularity strength $R(\theta)$ obtained from this solution is in excellent agreement with that obtained by Levy et al. [5], fig. 18a. The displacement solution was such that the difference between the local s components of displacement of the two crack tip nodes of a near tip element

$$U^- = U_I - U_J$$

was from 10 to 100 times greater than the difference between local t components

$$V^- = V_I - V_J$$

in the region $\theta > 45°$. The stresses presented are those at $s/s^* = 1/4$, $\tan\psi/\tan\alpha = \mp 1/2$. These two inner element states are connected by a straight line in figs. (18b - g). The shear stress distribution is in reasonably good agreement with the Prandtl distribution, fig. 18b. There are enormous variations

of normal stresses σ_{xx}, σ_{yy}, $\sigma_{xx} + \sigma_{yy} + \sigma_{zz}$, about the Prandtl field in the fan region while in the range $\theta < 45°$ the stresses are larger than the Prandtl prediction, figs. (19c - e). The latter behavior was found in procedure B above. Elasticity prevails in the range $\theta > 135°$. The deviatoric stresses S_{xx}, S_{yy} are plotted in figs. (18f,g). They agree very well with the Prandtl field in the fan - a fact which explains how an excellent $R(\theta)$ solution could accompany an unrealistic normal stress distribution.

It is easy to see how the large normal stress variation within an element is possible by looking at the dilatational strain field within an element:

$$2\epsilon_{KK} = (v^- - u^- \tan\psi)\cot\alpha/s + \text{const} \qquad (17)$$

Since u^- was at least ten times greater than v^- the terms v^- and $u^- \tan\psi$ are comparable even for the small angle of $\psi = 3.75°$ which has a tangent equal to 0.065. Hence the change in sign of $\tan\psi$ in going from one integration station to its image about $\psi = 0$ accounts for the large dilatational variation found.

Doing a Mohr's circle rotation of angle $-\theta$ from the local strain components ϵ_{ss}, ϵ_{tt}, γ_{st} to the global components shows how the reasonable $R(\theta)$ resulted in the fan from the displacement solution:

$$2\gamma_{xy} = \{(u^- \cos 2\theta - v^- \sin 2\theta) - (u^- \sin 2\theta + v^- \cos 2\theta)\tan\psi\}\cot\alpha/s + \text{const} \qquad (18)$$

Coupling the facts that over most of the fan

$$u^- \gg v^-$$
$$O(\cos 2\theta) = O(\sin 2\theta)$$

we can say

$$2\gamma_{xy} \approx \{u^-(\cos 2\theta - \sin 2\theta \tan\psi)\}\cot\alpha/s \qquad (19)$$

The term $\sin 2\theta \tan\psi$ is obviously negligible compared to $\cos 2\theta$ over most of the fan hence

$$2\gamma_{xy} \approx u^{-} \cot N\alpha \cos 2\theta / s \qquad (20)$$

there. The solution found u^{-} approximately even about $\theta = 90^{\circ}$ hence the even distribution of $R(\theta)$ about this line, fig. 18a. Although the confusing stress and strain results of this procedure can be easily explained in terms of the displacement solution it is difficult to rationalize why this procedure induces an excellent displacement solution.

The most disturbing feature of the five procedures outlined above is the seemingly strong influence the elastic crack tip stress solution has on the resulting plastic crack tip stress solution. In an attempt to elucidate this phenomenon it was decided to use the elastic singularity interpolation function, eq. (6), to gain the elastic solution and then switch to the isoparametric interpolation function for the plastic increments. With the integration procedure issue basically unresolved, the procedure A which gave reasonable results with mesh I except for an erratic $R(\theta)$ curve was chosen along with mesh II with the hope that the extra degrees of freedom would correct the $R(\theta)$ curve. The elastic solution was everywhere within 2% of the exact solution as reported separately in a recent paper by Tracey [7]. The elastic solution gained from using the dual singularity interpolation function, eq. (7), procedure A and mesh II appears in figs. 19 along with the nearly exact elastic solution and that isoparametric solution using procedure A and mesh I presented earlier. Surprisingly the dual singularity formulation and the isoparametric result, resemble the Prandtl distribution. In the round bar problem these formulations were similar but they were closer to the exact elastic than the Prandtl solution; of course the round bar problem used the integration procedure D .

The elastic-plastic solution was solved by ten plastic increments of $0.1\ K_o$ and then fifteen increments of $0.2\ K_o$ so that a total load of $K = 5.0\ K_o$ was reached. The resulting near tip stress solution is plotted in figs. (20a,b,c). The sh ape of the stress distributions resemble the exact elastic distribution more than the Prandtl; the shear stress is the best evidence of this. The associated crack tip solution had the peculiar and physically unreasonable feature of a negative u_y over the range $0^{\circ} < \theta < 90^{\circ}$, fig. 20d. This feature suggests that the coincident crack tip nodes are "too free" and perhaps should be

constrained to the specific relative motion expected from a $1/r$ shear singularity. This feeling motivated consideration of the previous problem modified by adding the constraint

$$V_I = V_J$$

for each near tip element. This constraint in conjunction with integration procedure A disallows a singular dilatation while allowing a singular shear strain whose strength is proportional to $(u_I - u_J)$. The load was increased to $K = 4.1\ K_o$ in 31 increments of $0.1\ K_o$. The crack tip displacement solution appears in figs. (21a,b). The unreasonable negative u_y values at $r = 0$ disappear by employing the constraint although the slope of the displacement distribution is oscillatory in the region $45° < \theta < 135°$. This latter effect is evidenced by the $R(\theta)$ curve of fig. 21c. The stress solution, figs. (21d,e,f), is very close to the Prandtl solution over $0 < \theta < 120°$. Elasticity prevails over $\theta > 150°$. The region $120° < \theta < 150°$ resembles a constant state region. This is the only solution obtained so far which has distinctly different elastic and plastic stress solutions each of which are reasonable. The one worrisome detail of this solution is the oscillations in the crack tip displacements.

dwa

References

1) M. L. Williams, "On the Stress Distribution at the Base of a Stationary Crack", J. Appl. Mech., vol. 24, p. 109, 1957.

2) J. R. Rice, "A Path Independent Integral and the Approximate Analysis of Strain Concentration by Notches and Cracks", J. Appl. Mech., vol. 35, p. 379, 1968.

3) J. W. Hutchinson, "Singular Behavior at the End of a Tensile Crack in a Hardening Material", J. Mech. Phys. Solids, vol. 16, p. 13, 1968.

4) J. R. Rice and G. F. Rosengren, "Plane Strain Deformation Near a Crack Tip in a Power Law Hardening Material", J. Mech. Phys. Solids, vol. 16, p. 1, 1968.

5) N. Levy, P. V. Marcal, W. J. Ostergren, and J. R. Rice, "Small Scale Yielding Near a Crack in Plane Strain: A Finite Element Analysis" to appear in Int'l. J. Fracture Mech., 1971.

6) P. V. Marcal and I. P. King, "Elastic-Plastic Analysis of Two-Dimensional Stress Systems by the Finite Element Method", Int'l. J. Mech. Sciences, vol. 9, p. 143, 1967.

7) D. M. Tracey, "Finite Elements for Determination of Crack Tip Elastic Stress Intensity Factors", to appear in Engin. J. Fracture Mech., 1971.

8) R. T. Shield, "On the Plastic Flow of Metals Under Conditions of Axial Symmetry", Proc. Roy. Soc. A233, p. 267, 1955.

9) C. H. Lee and Shiro Kobayashi, "Elastoplastic Analysis of Plane-Strain and Axisymmetric Flat Punch Indentation by the Finite Element Method", Int'l. J. Mech. Sciences, vol. 12, p. 349, 1970.

10) J. R. Rice and M. A. Johnson, "The Role of Large Crack Tip Geometry Changes in Plane Strain Fracture", in Inelastic Behavior of Solids (M. F. Kanninen et al., Eds.), McGraw-Hill, New York, p. 641, 1970.

11) H. D. Hibbitt and P. V. Marcal, "Hybrid Finite Element Analysis With Particular Reference to Axisymmetric Structures", AIAA paper No. 70-137, presented at the AIAA 8th Aerospace Sciences meeting, 1970.

12) W. J. Ostergren, "Small Scale Yielding Near a Crack in Plane Strain: A Finite Element Analysis", M. S. Thesis, Brown University, 1969.

13) N. Levy, "Application of the Finite Element Method to Large Scale Elastic-Plastic Problems of Fracture Mechanics", Ph.D. Thesis, Brown Univ., 1969.

14) H. F. Bueckner, "Coefficients for Computation of the Stress Intensity Factor K_I for a Notched Round Bar", in Fracture Toughness Testing and Its Applications, ASTM STP 381, Am. Soc. Testing Matls., 1965, p. 82.

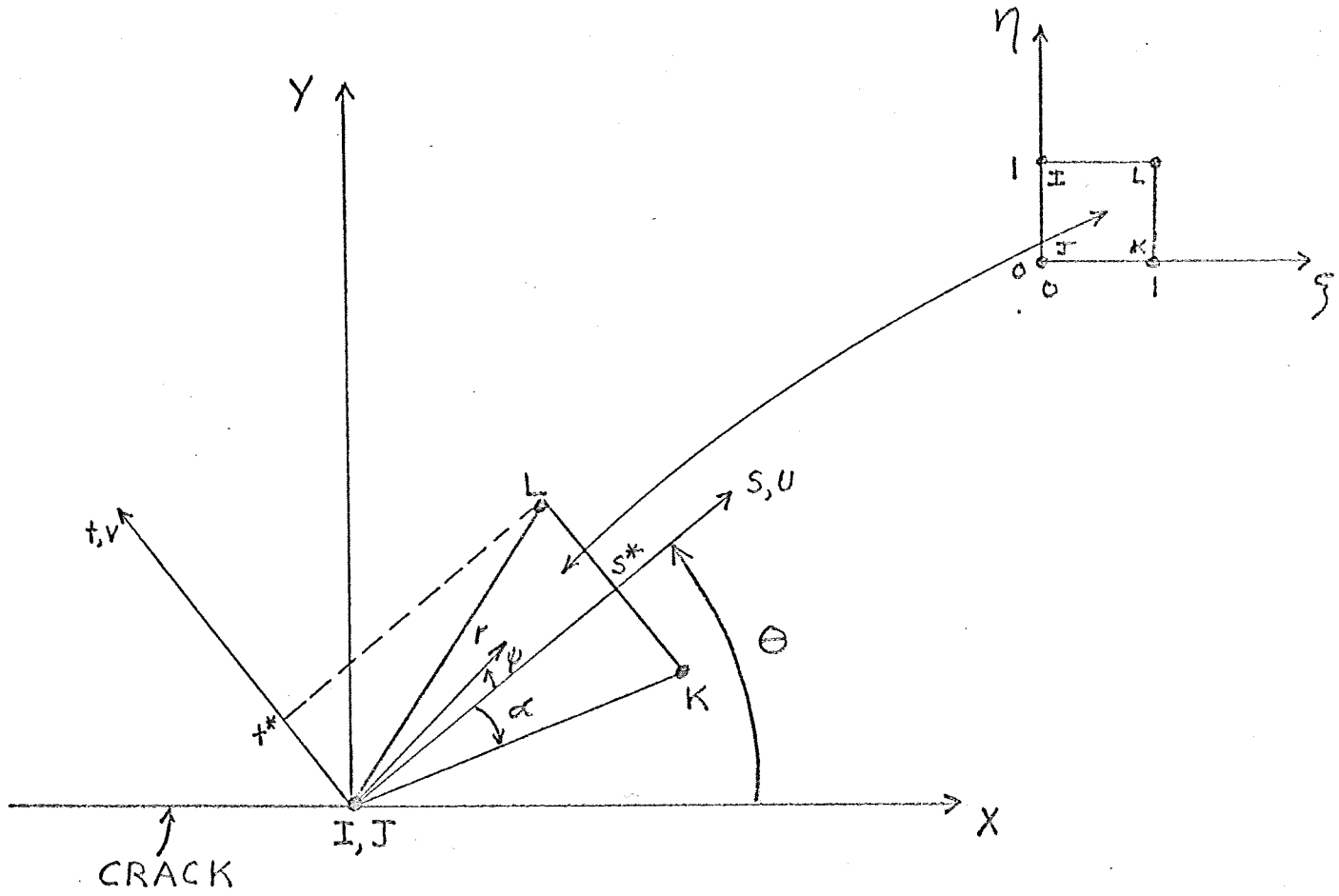

FIG. 1 A NEAR TIP TRAPEZOIDAL ELEMENT

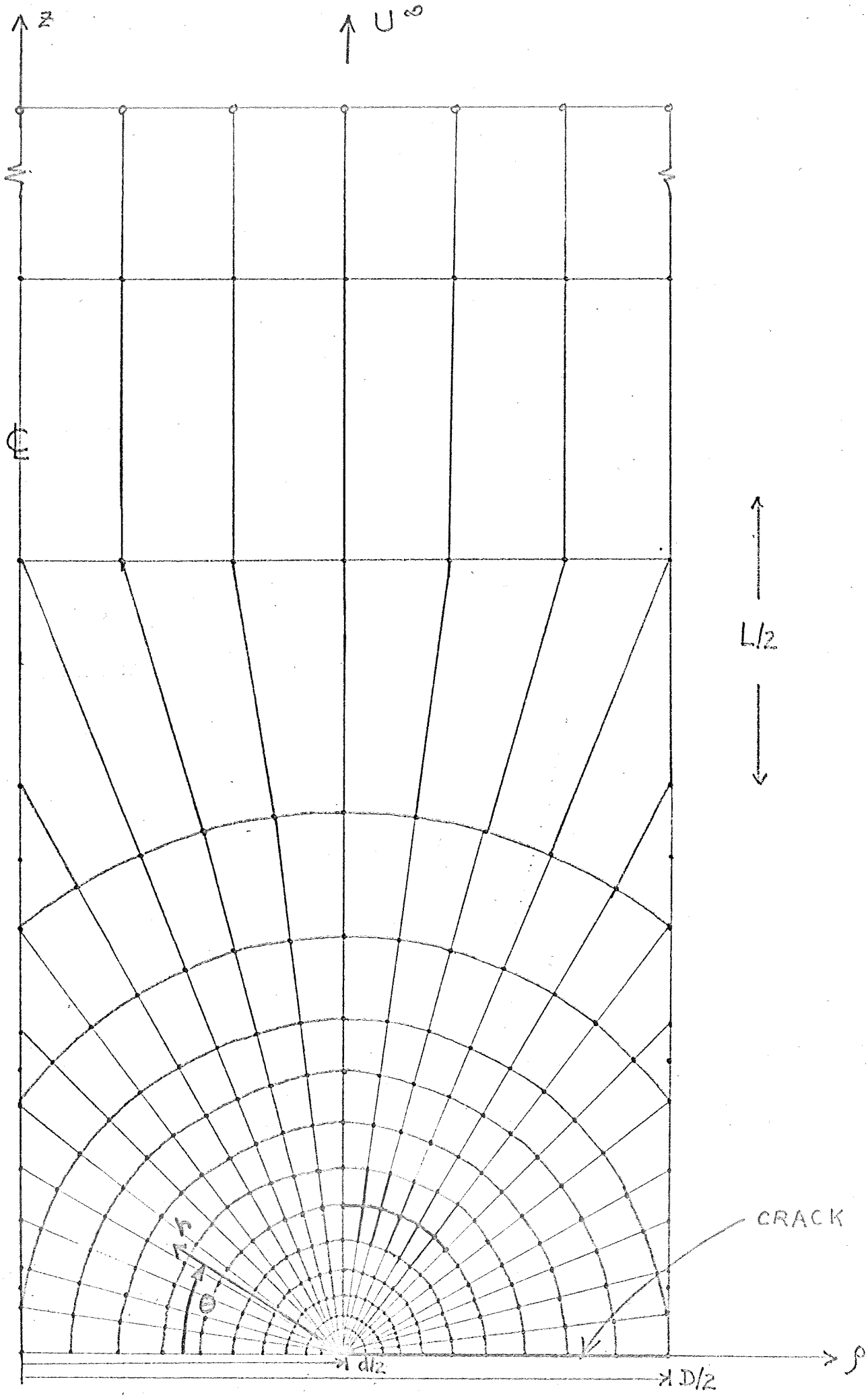

FIG. 2 MESH FOR ROUND BAR

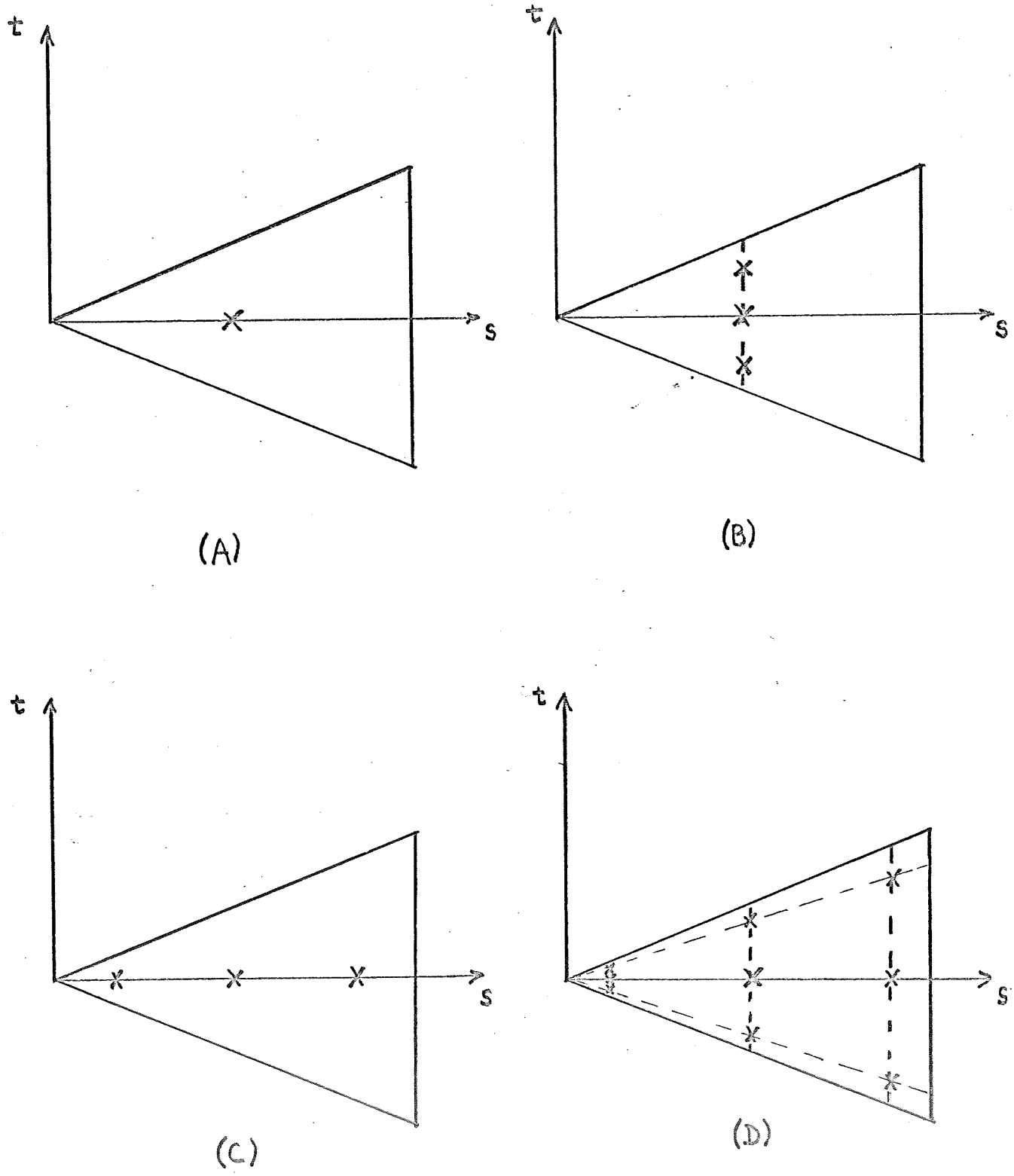

FIG. 3 INTEGRATION STATIONS IN (s,t) PLANE FOR PROCEDURES A, B, C, D

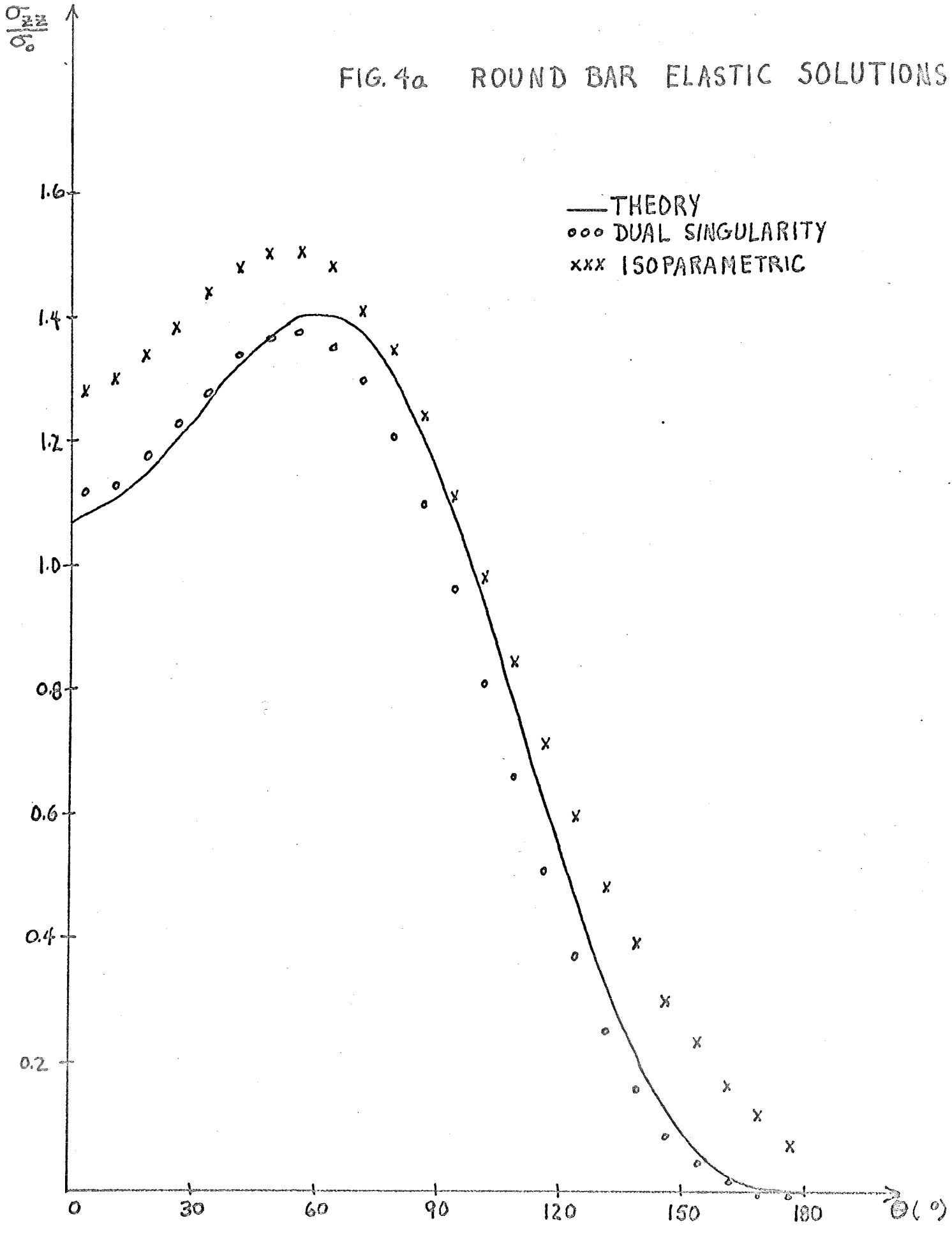

FIG. 4a ROUND BAR ELASTIC SOLUTIONS

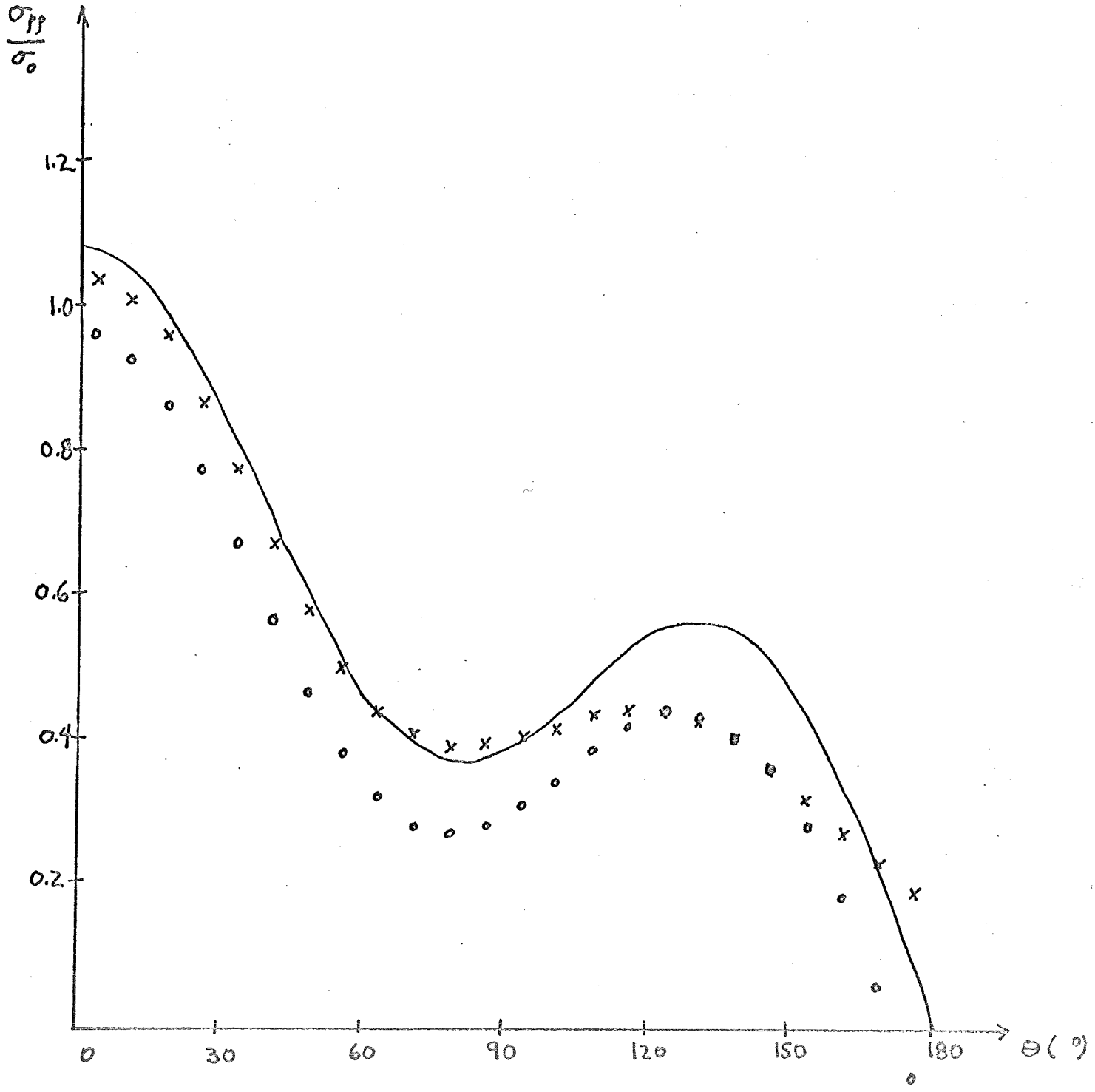
$\frac{\sigma_{\theta\theta}}{\sigma_0}$
1.2
1.0
0.8
0.6
0.4
0.2
0
30
60
90
120
150
180
θ(°)

FIG. 4 b

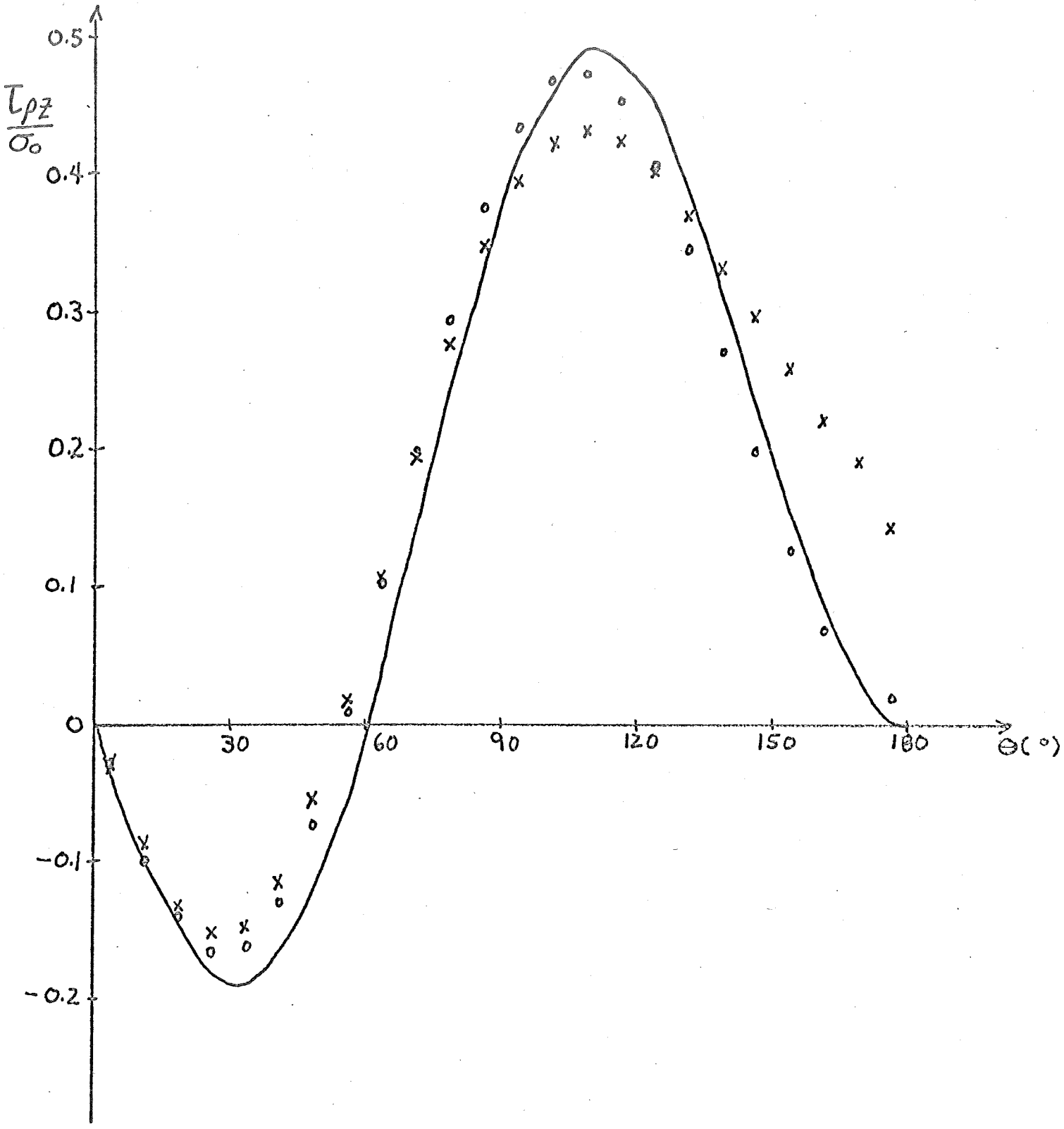

FIG. 4c

FIG. 5 LOAD-DEFLECTION CURVE FOR ROUND BAR

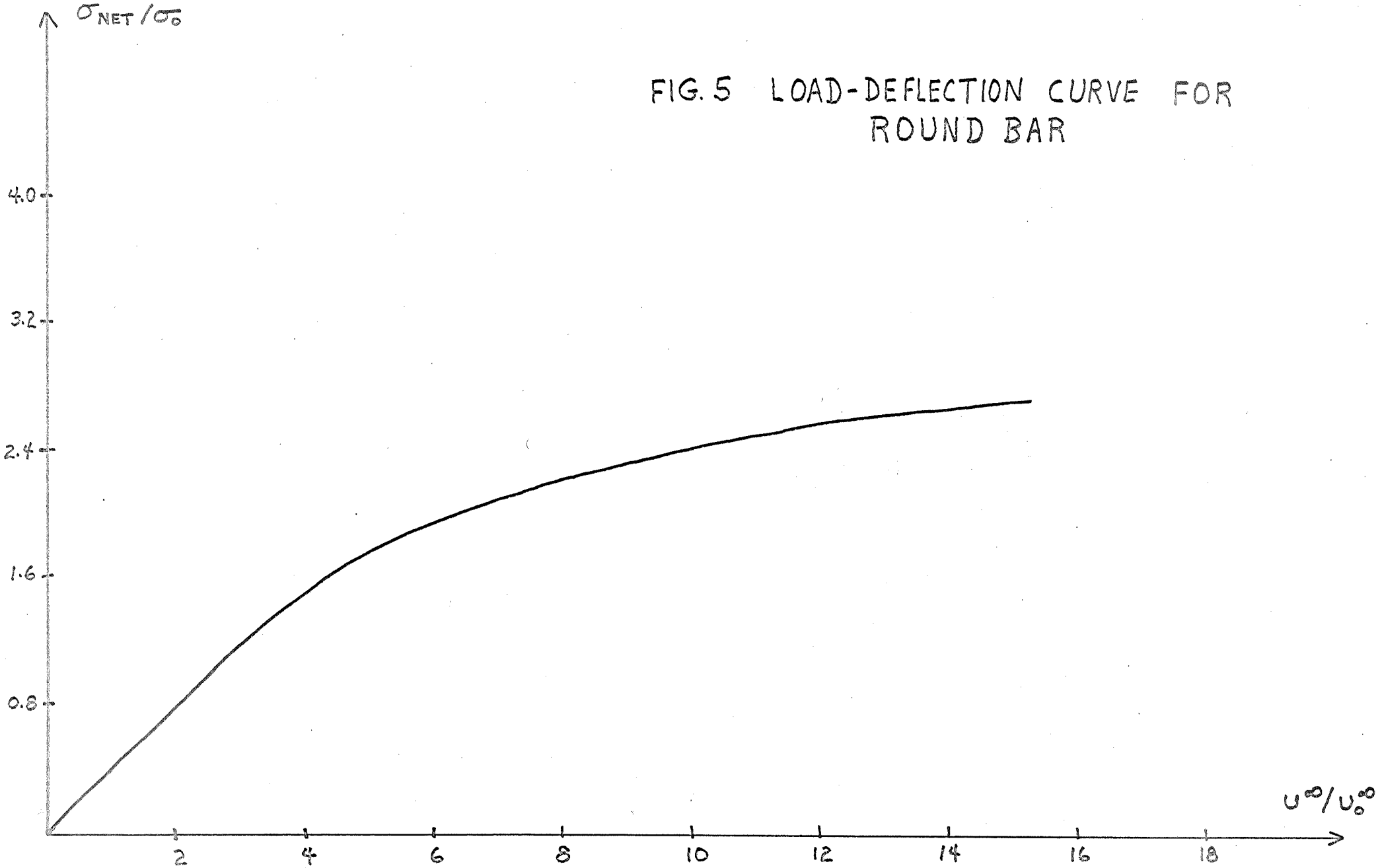

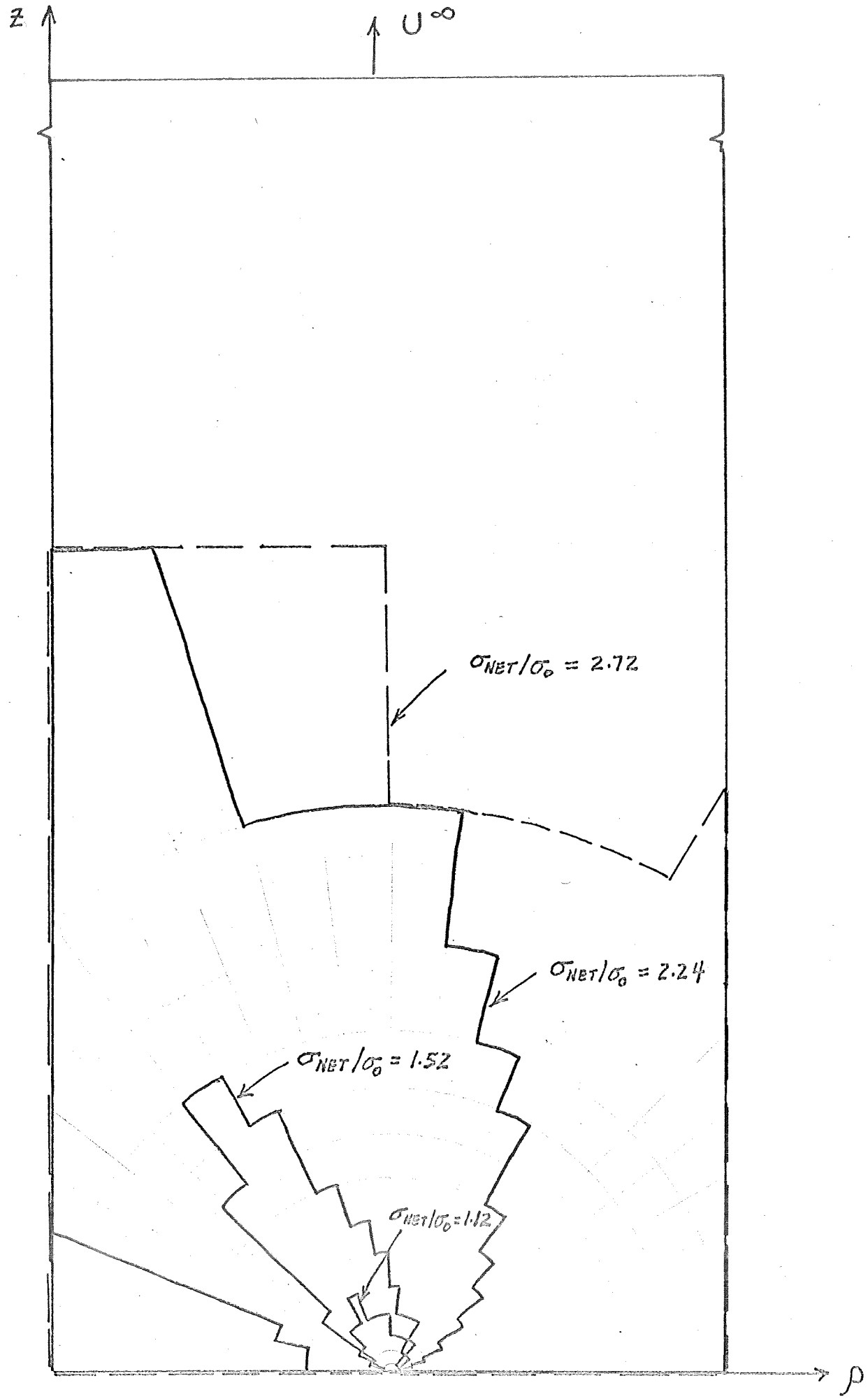

FIG. 6 ROUND BAR ELASTIC-PLASTIC BOUNDARIES

FIG. 7 NET SECTION STRESS AT LIMIT LOAD

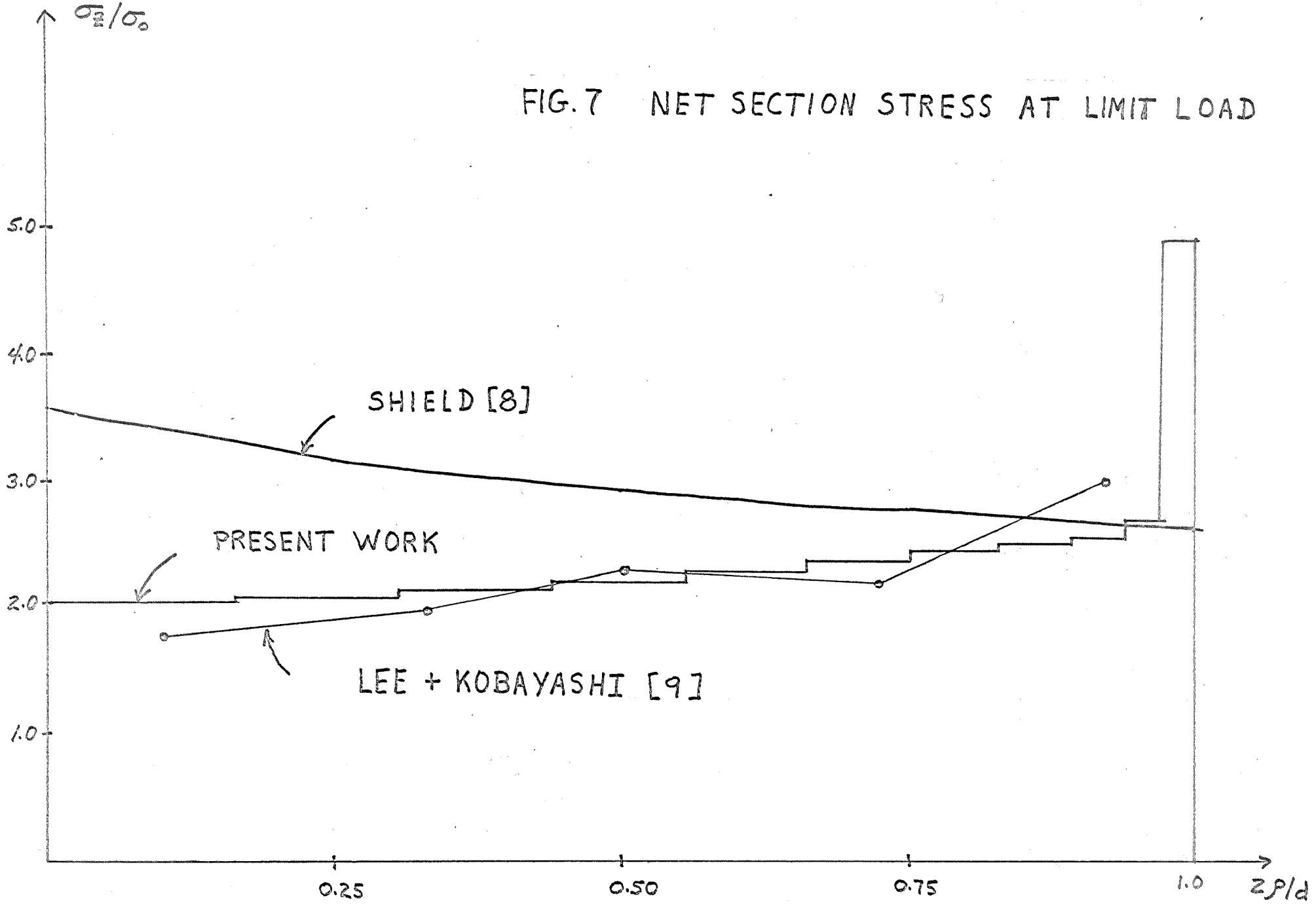

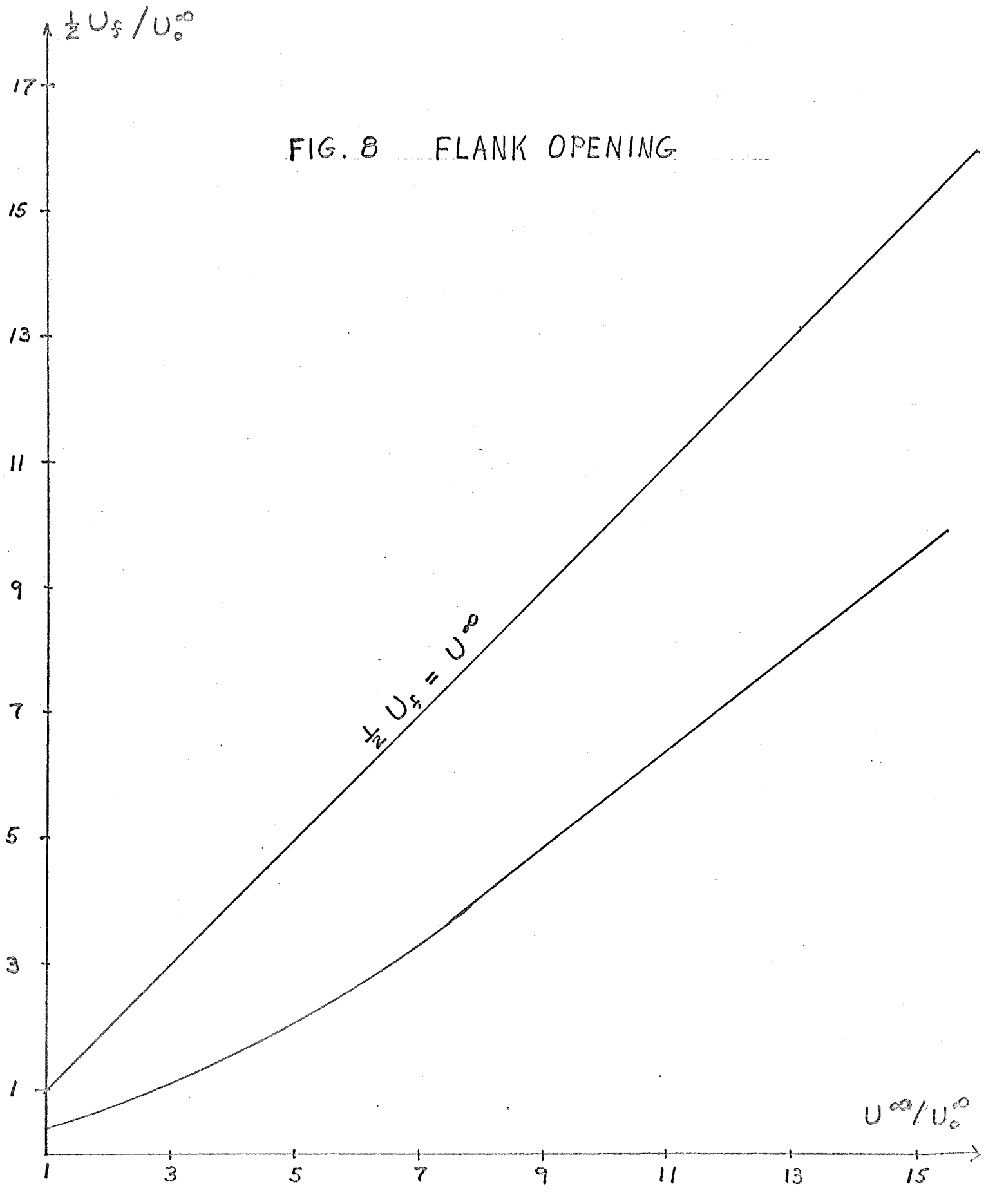

FIG. 8 FLANK OPENING

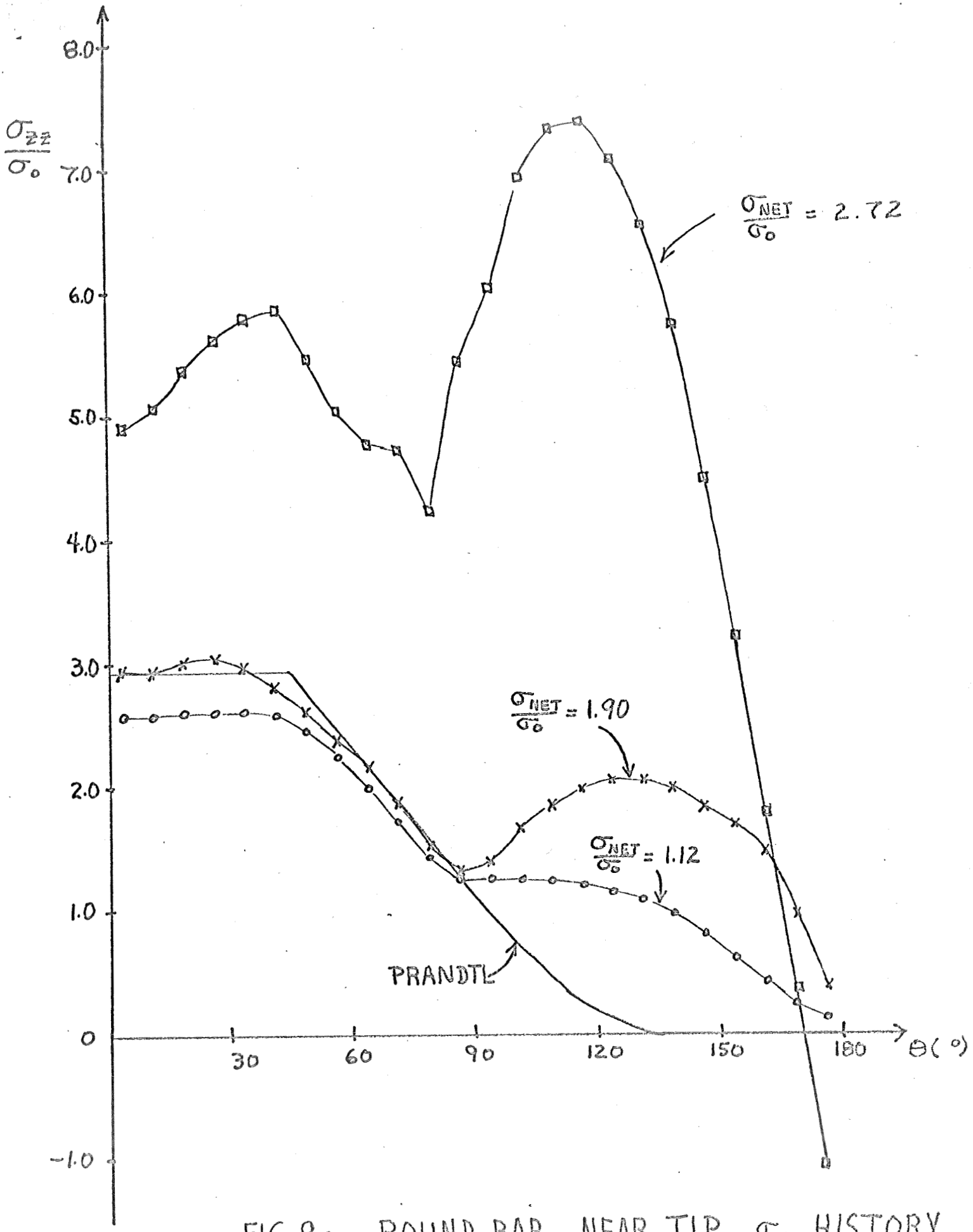

FIG. 9a ROUND BAR NEAR TIP σ_{zz} HISTORY

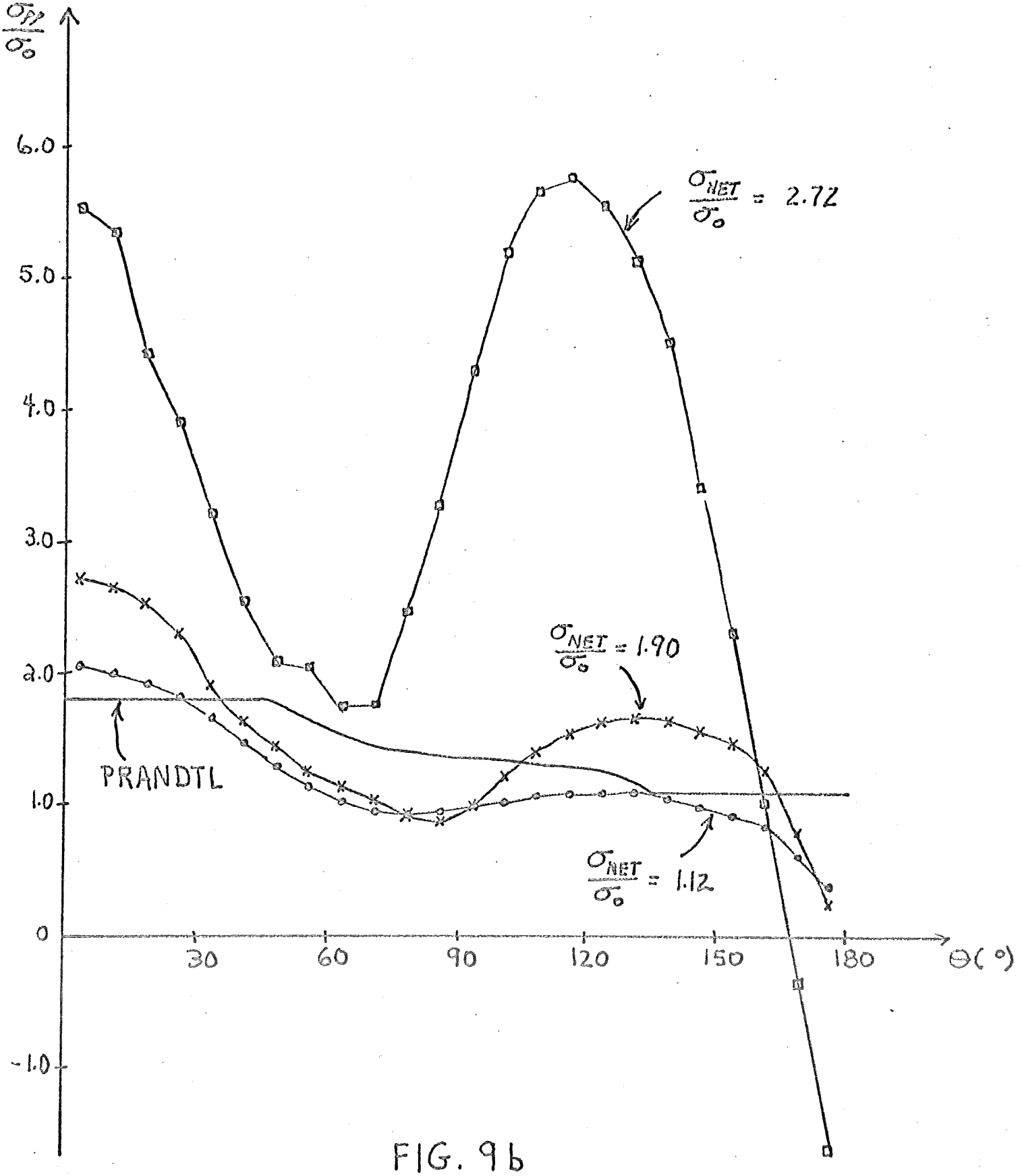
$\frac{\sigma_{yy}}{\sigma_o}$
6.0
5.0
4.0
3.0
2.0
1.0
0
-1.0
30
60
90
120
150
180
Θ(°)
$\frac{\sigma_{NET}}{\sigma_o}$ = 2.72
$\frac{\sigma_{NET}}{\sigma_o}$ = 1.90
$\frac{\sigma_{NET}}{\sigma_o}$ = 1.12
PRANDTL

FIG. 9b

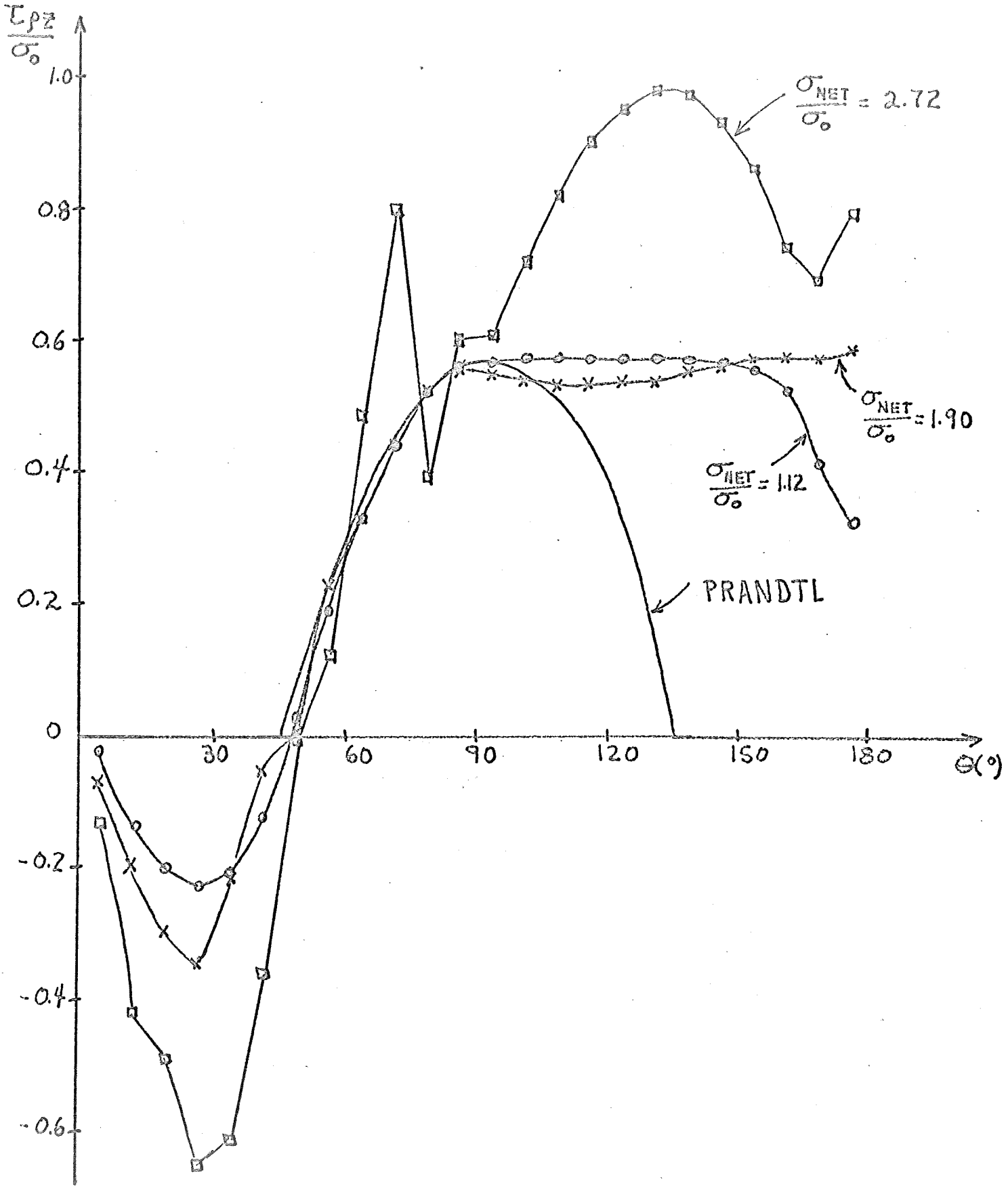
$\frac{\tau_{\rho z}}{\sigma_o}$
1.0
0.8
0.6
0.4
0.2
0
-0.2
-0.4
-0.6
30
60
90
120
150
180
θ(°)
$\frac{\sigma_{NET}}{\sigma_o}$ = 2.72
$\frac{\sigma_{NET}}{\sigma_o}$ = 1.90
$\frac{\sigma_{NET}}{\sigma_o}$ = 1.12
PRANDTL

FIG. 9c

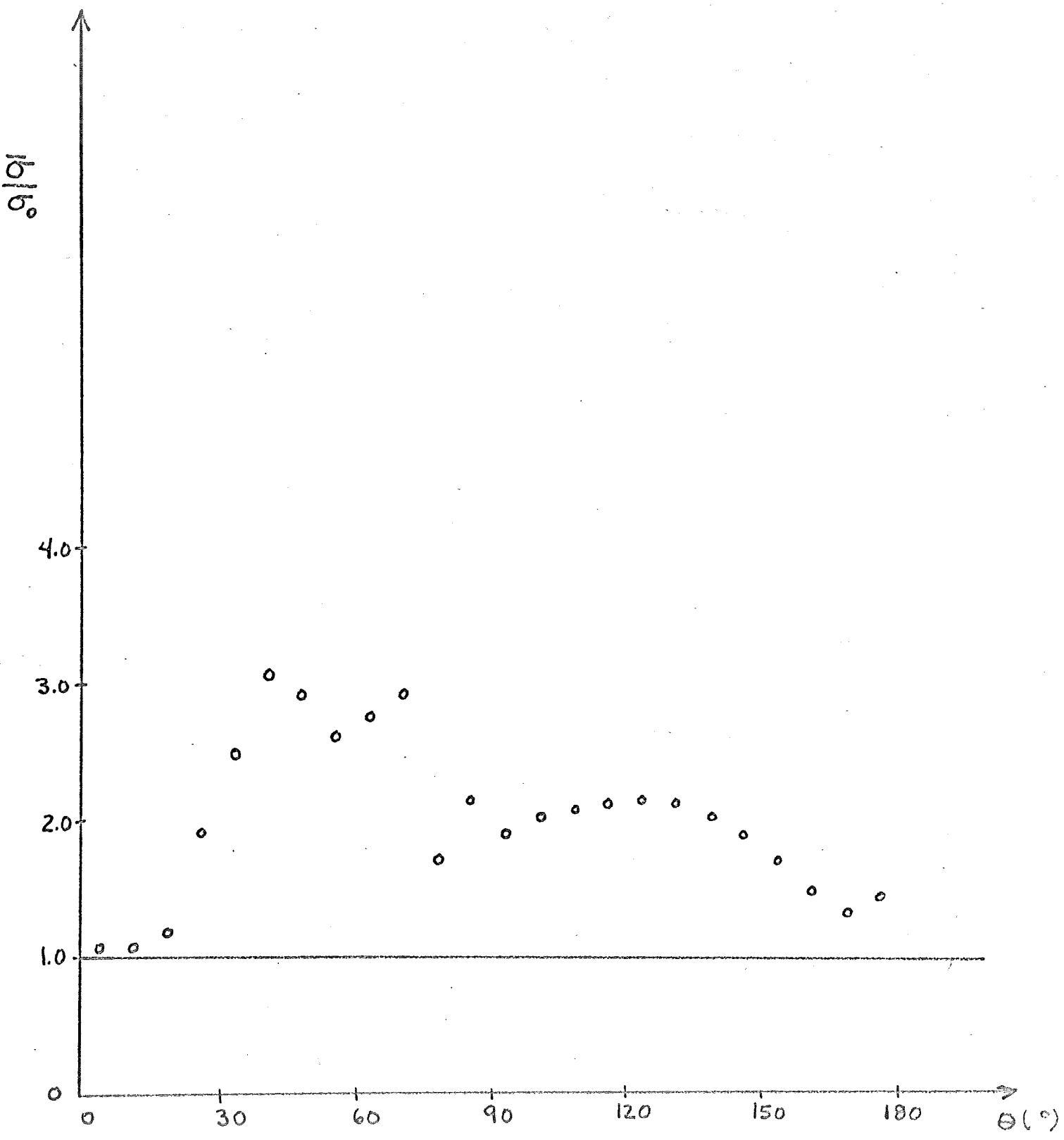

FIG. 10 EQUIVALENT STRESS ABOUT TIP AT $\sigma_{NET}/\sigma_0 = 2.72$

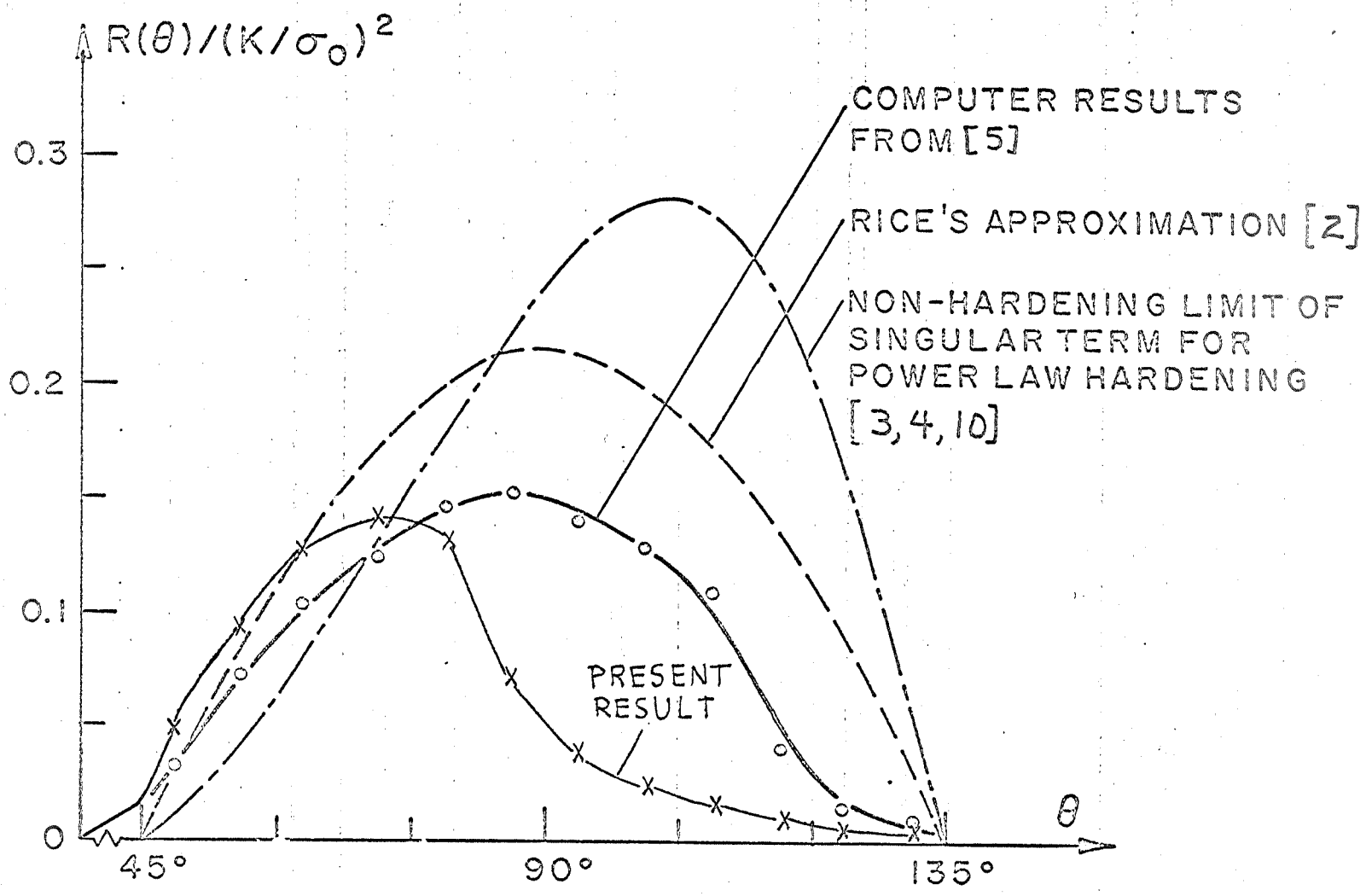

FIG 11 $R(\theta)$ ROUND BAR PROBLEM

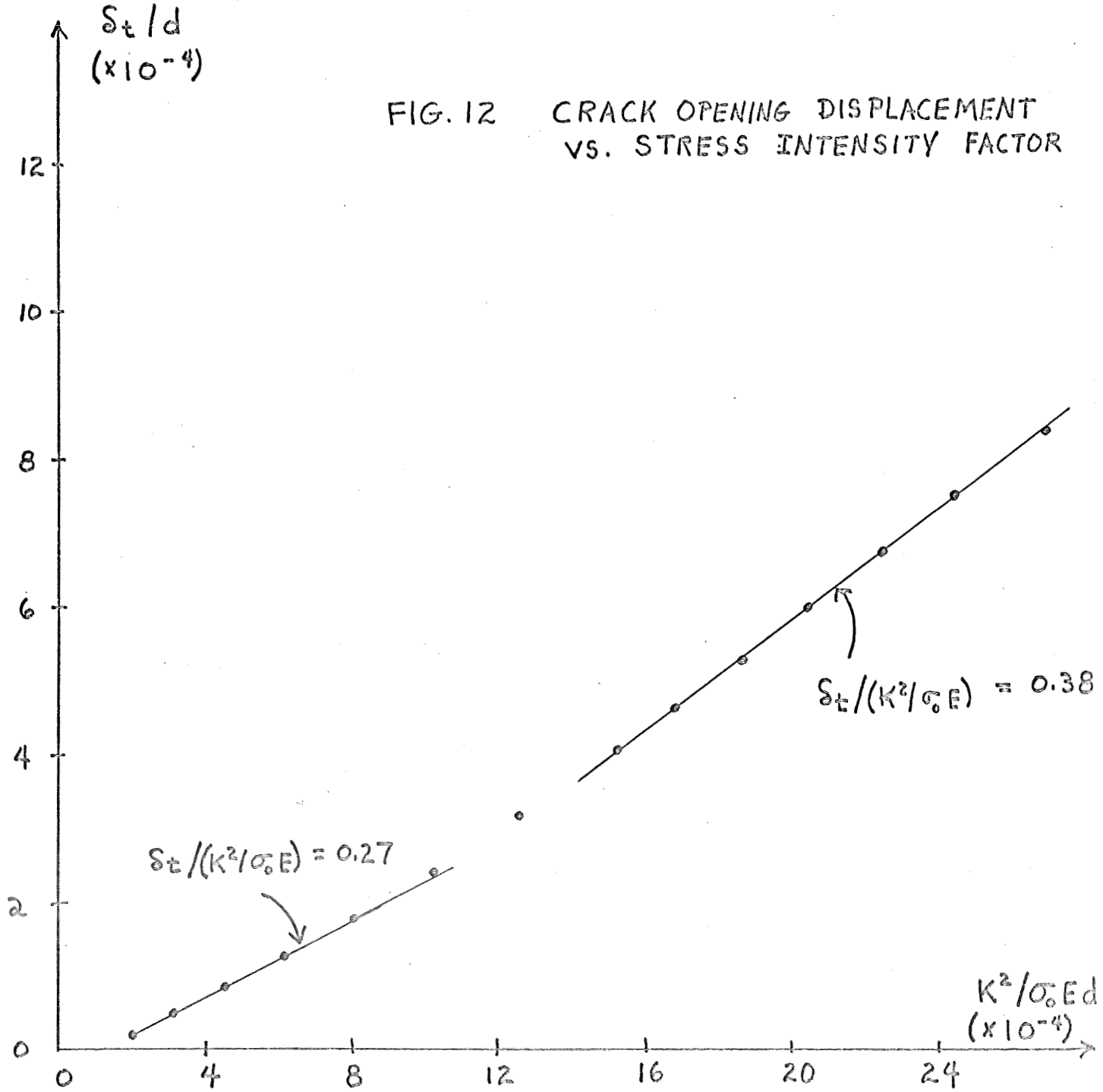

FIG. 12 CRACK OPENING DISPLACEMENT VS. STRESS INTENSITY FACTOR

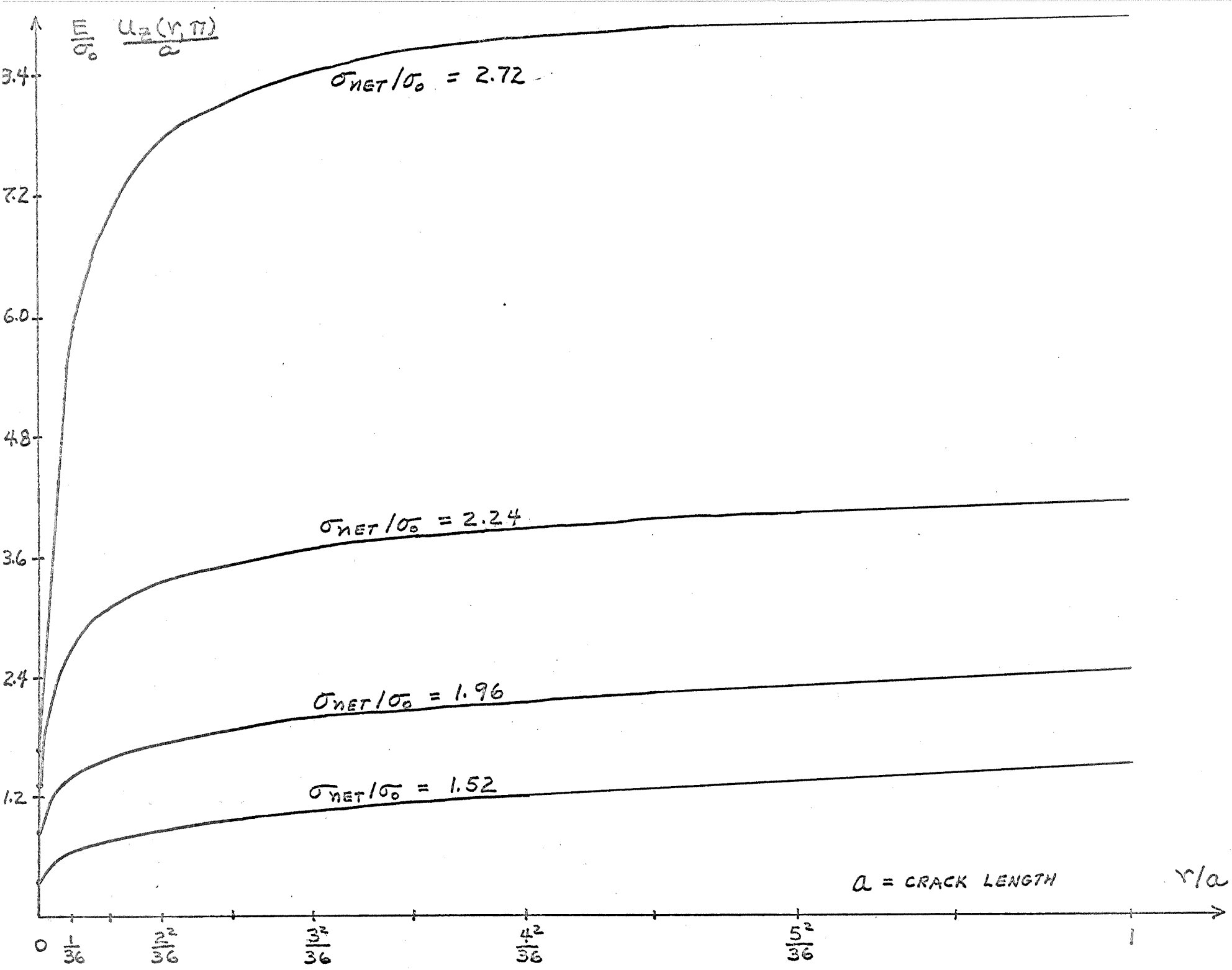

FIG. 13 DISPLACEMENT OF CRACK FACE

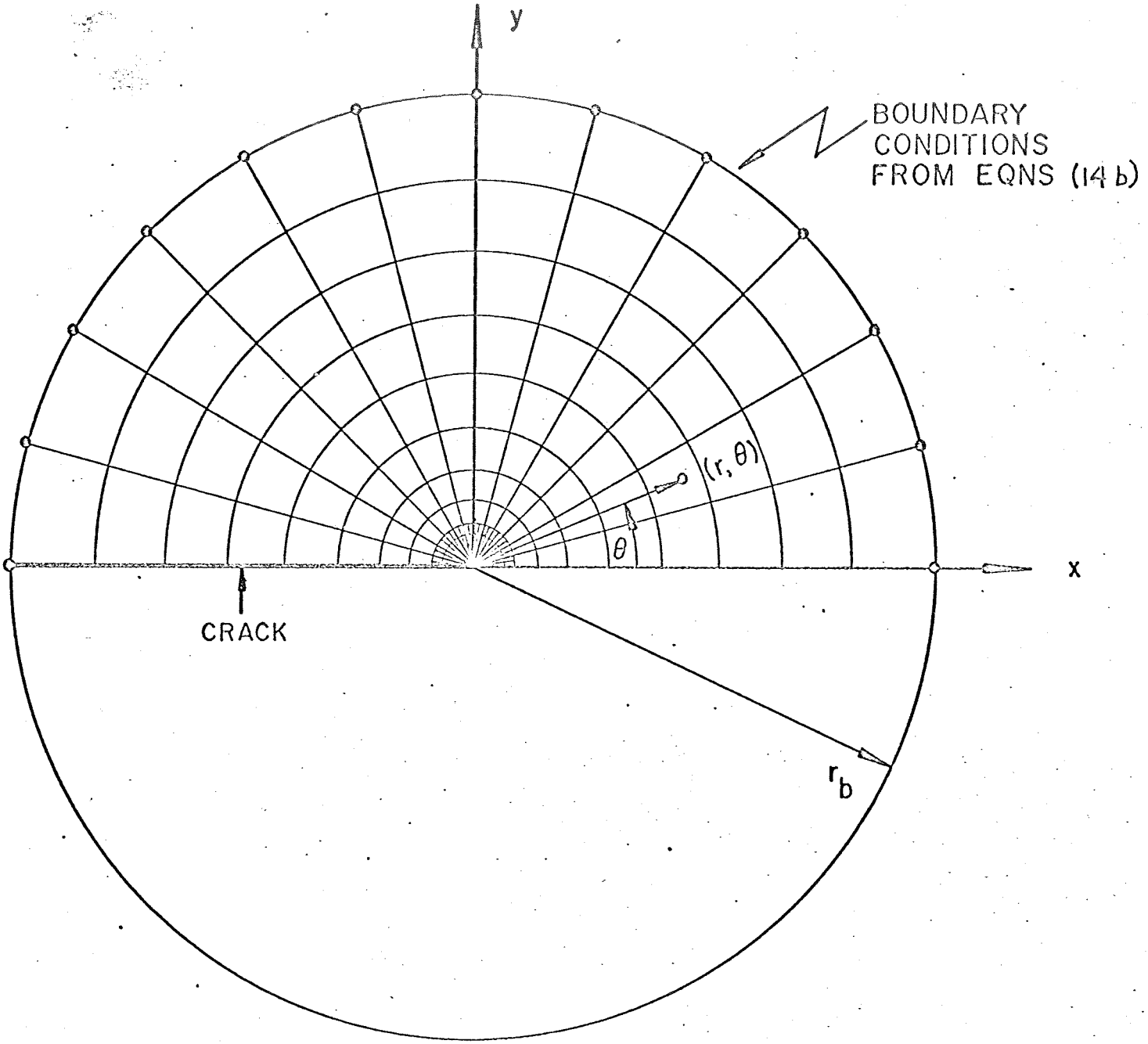

FIG. 14 FINITE ELEMENT TREATMENT OF
ASYMPTOTIC BOUNDARY VALUE PROBLEM

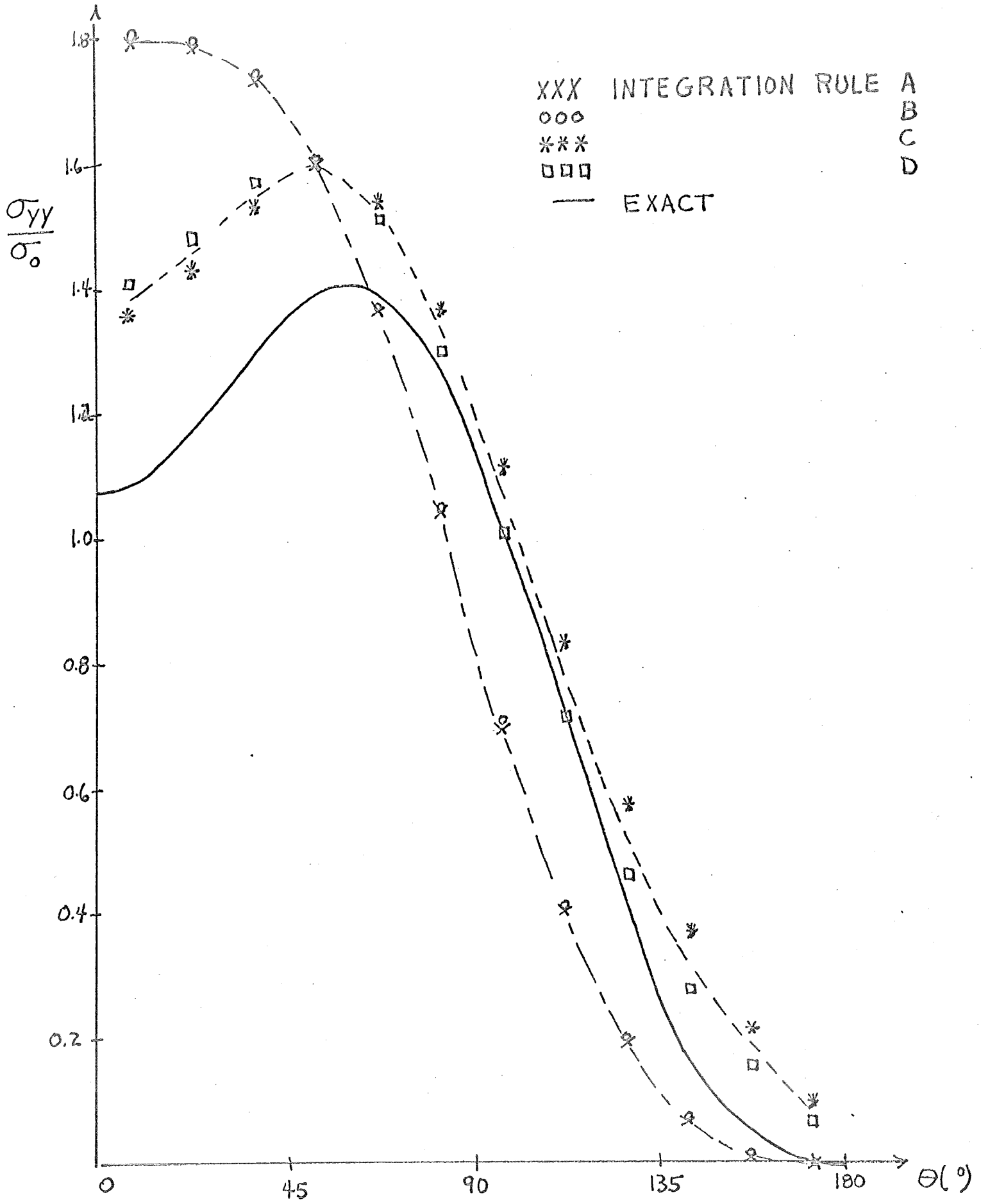
λ
1.8
1.6
1.4
1.2
1.0
0.8
0.6
0.4
0.2
σyy/σo
XXX INTEGRATION RULE A
ooo B
*** C
□□□ D
EXACT
0
45
90
135
180
θ(°)

FIG. 15a

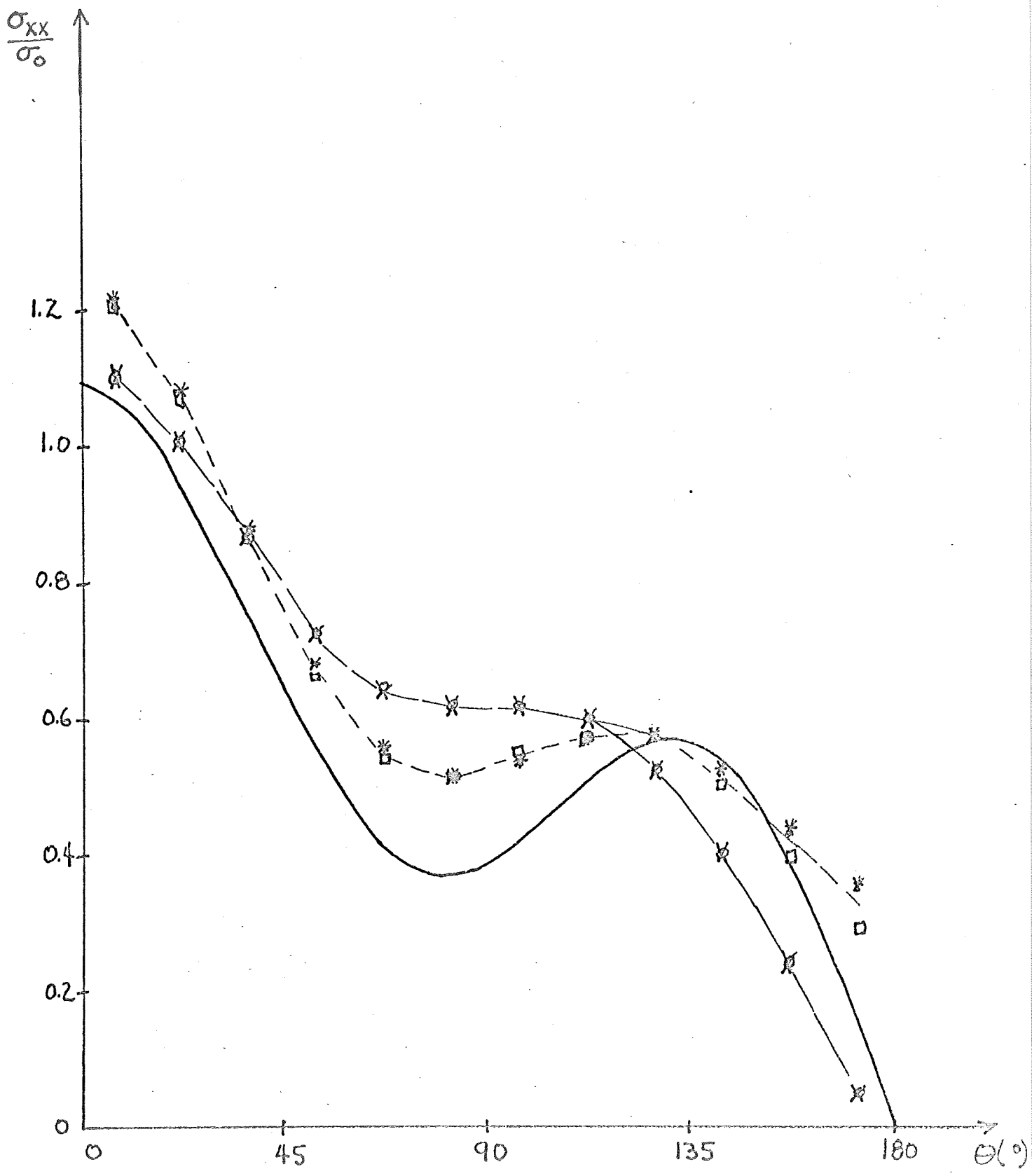

FIG. 15b

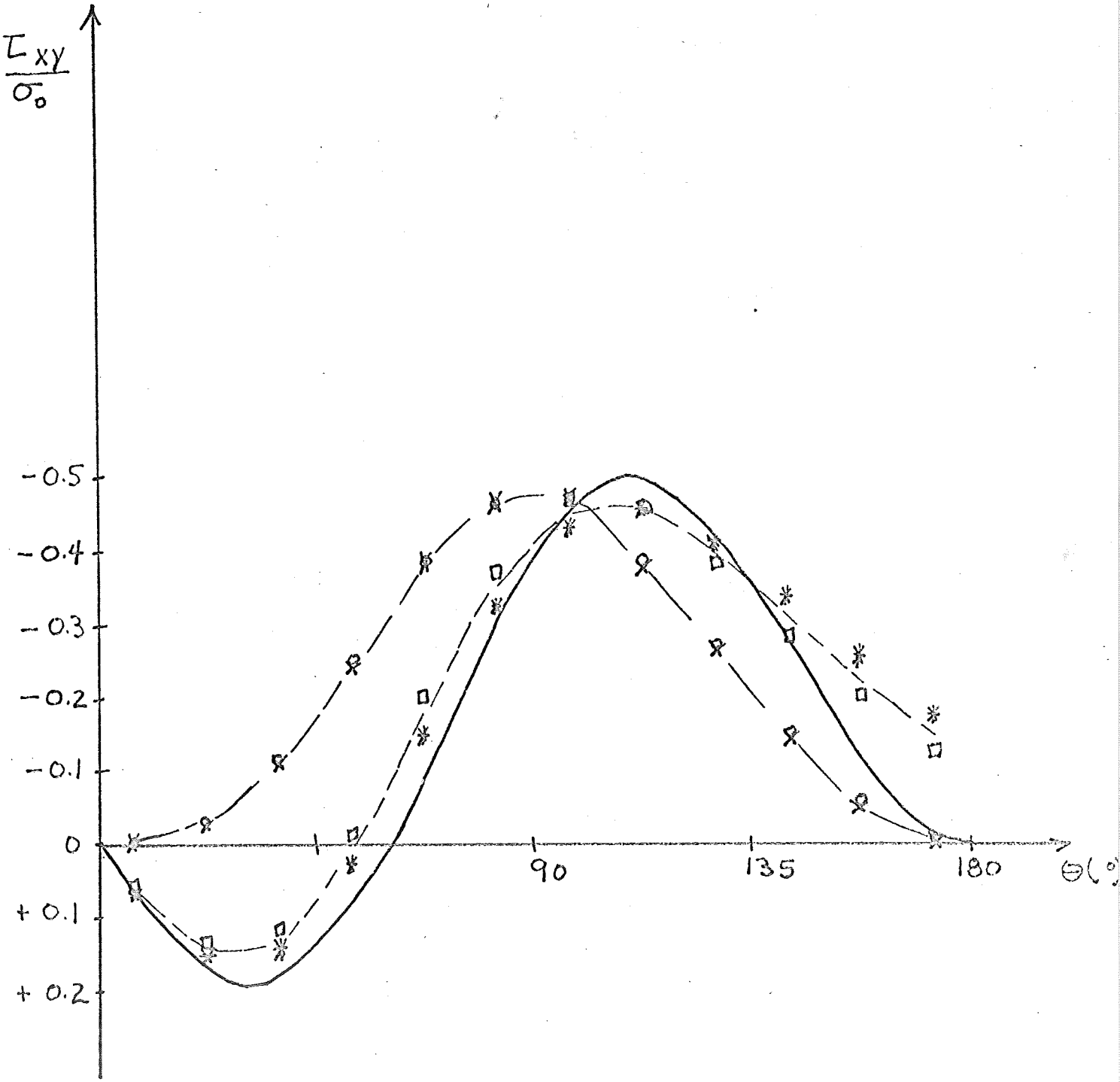

FIG. 15c

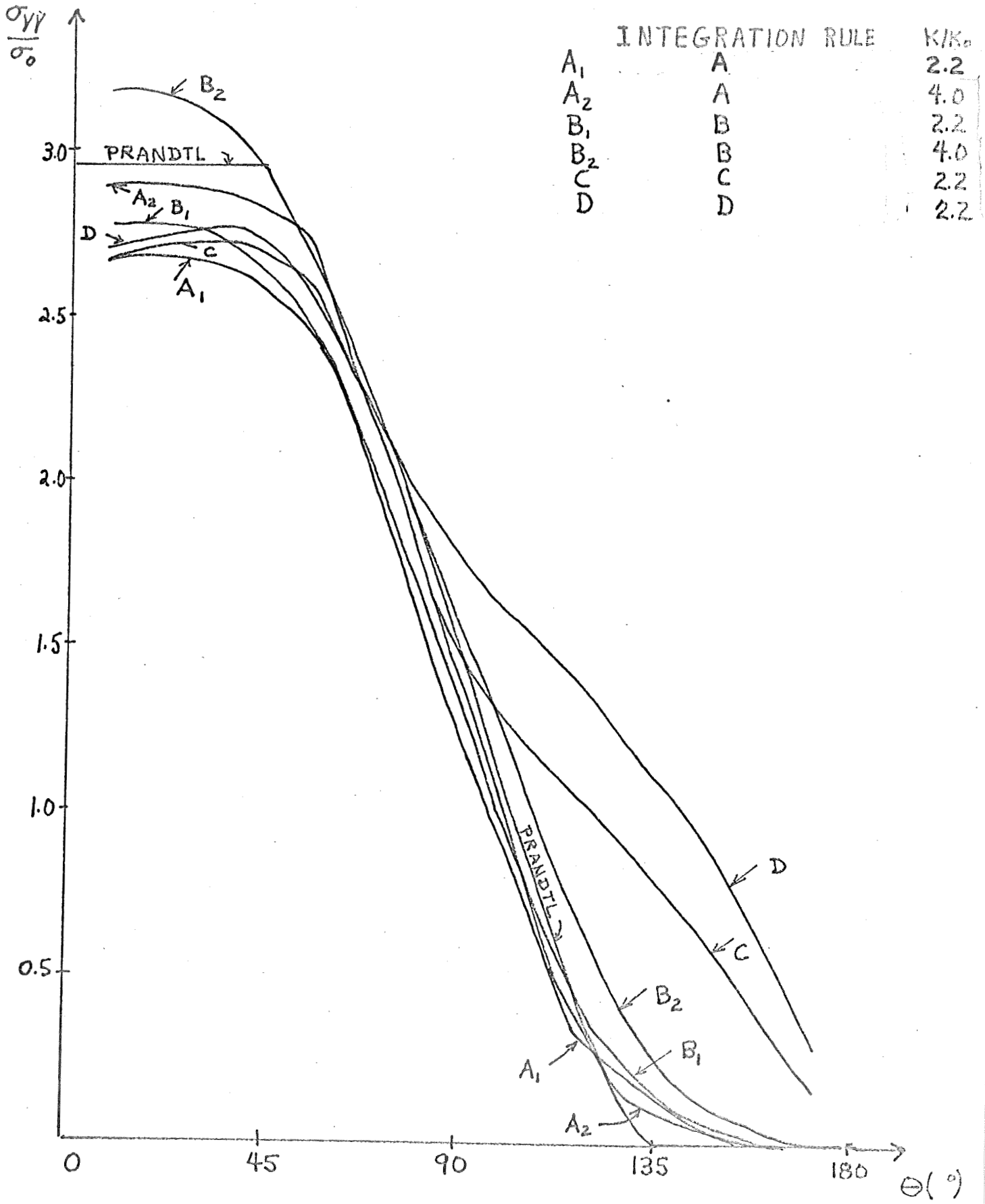
$\frac{\sigma_{yy}}{\sigma_0}$
INTEGRATION RULE
K/K₀
A₁ A 2.2
A₂ A 4.0
B₁ B 2.2
B₂ B 4.0
C C 2.2
D D 2.2
B₂
PRANDTL
A₂
B₁
D
C
A₁
3.0
2.5
2.0
1.5
1.0
0.5
0
45
90
135
180
θ(°)

FIG. 16a

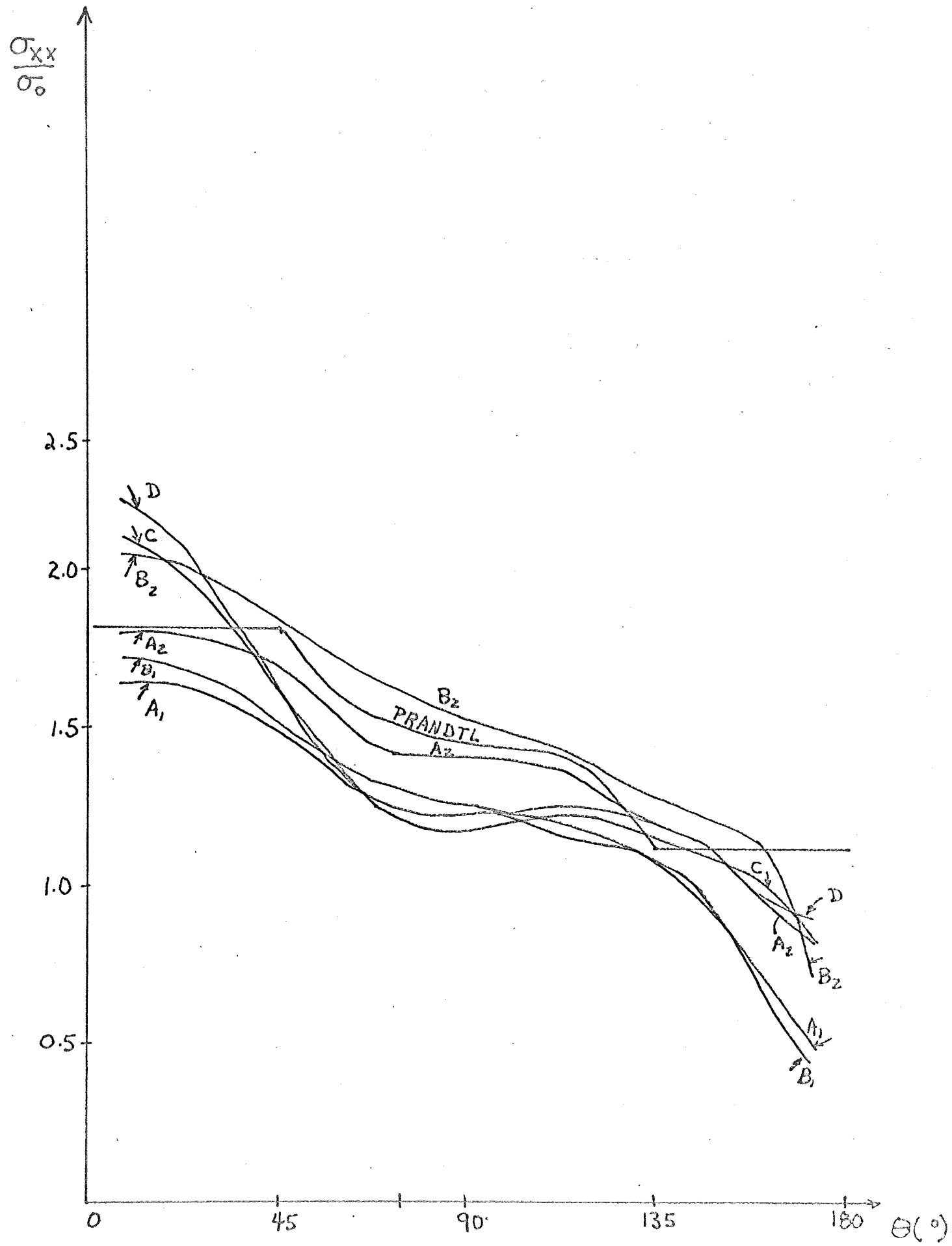
$\frac{\sigma_{xx}}{\sigma_o}$
2.5
2.0
1.5
1.0
0.5
0
45
90
135
180
θ(°)
D
C
B2
A2
B1
A1
PRANDTL
C1

FIG. 16 b

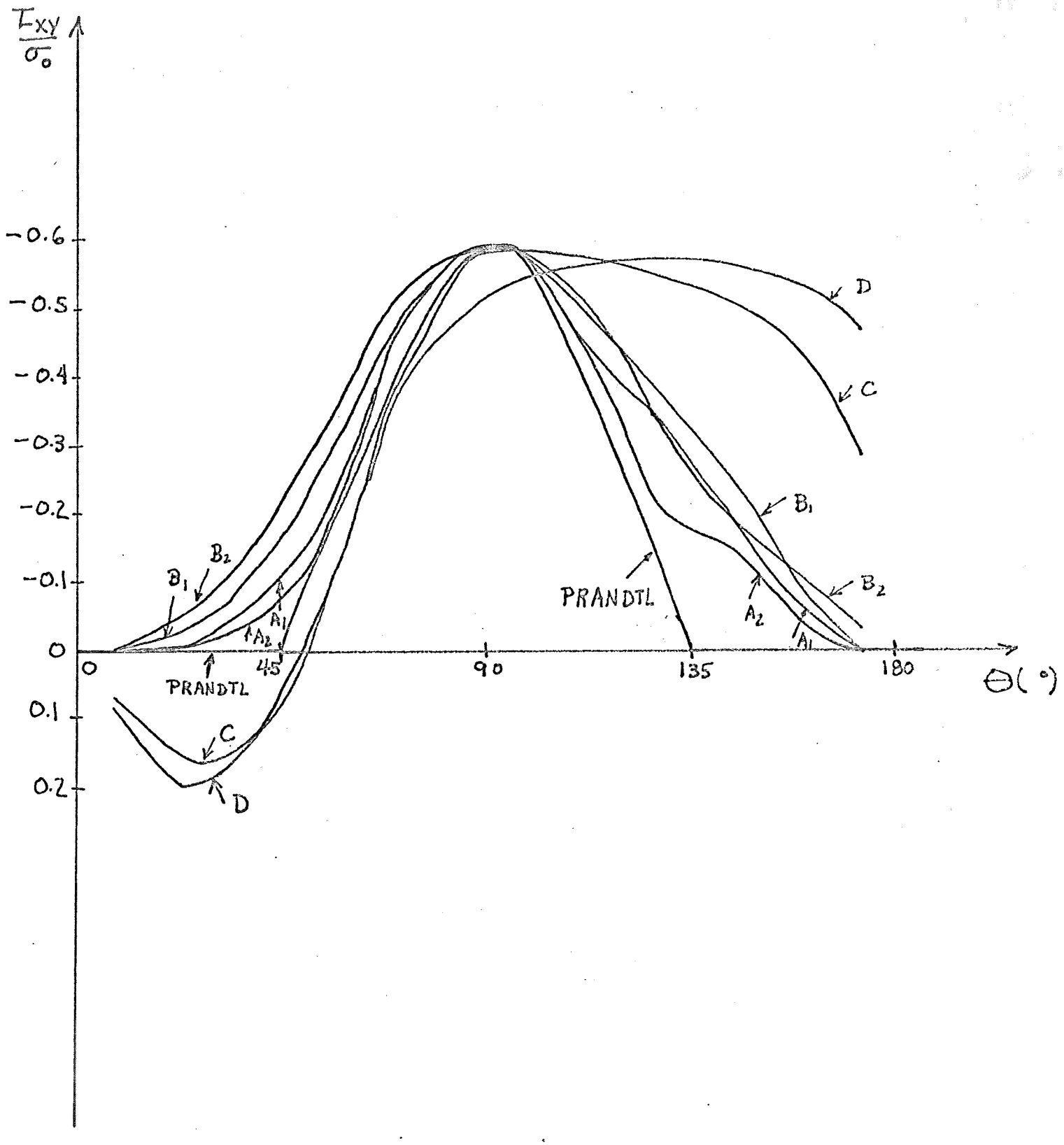
$\frac{\tau_{xy}}{\sigma_o}$
-0.6
-0.5
-0.4
-0.3
-0.2
-0.1
0
0.1
0.2
0
45
90
135
180
θ(°)
PRANDTL
PRANDTL
B_2
B_1
A_1
A_2
C
D
B_1
B_2
A_2
A_1
C
D

FIG. 16 C

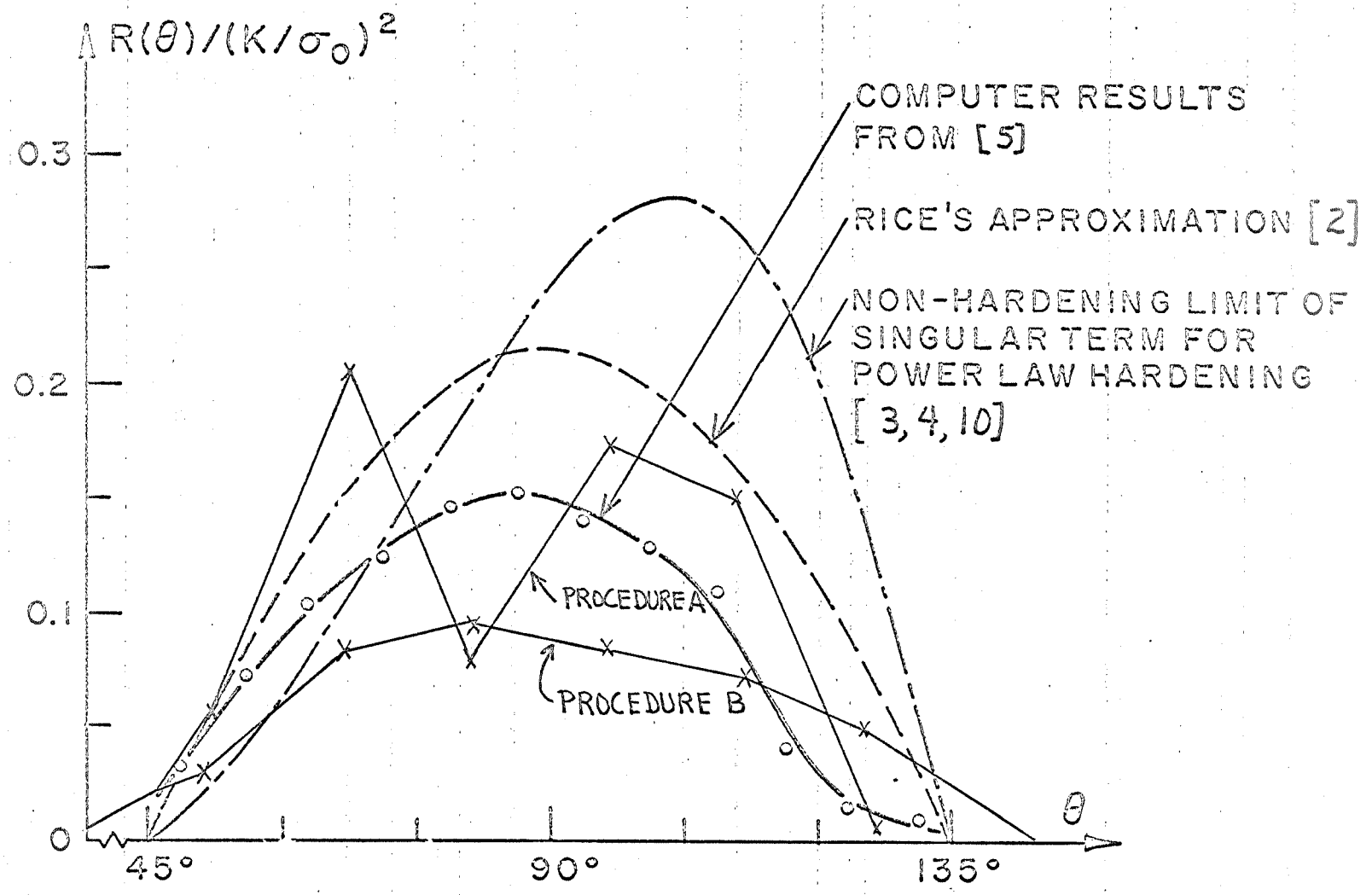
$\Delta R(\theta)/(K/\sigma_0)^2$
0.3
0.2
0.1
0
45°
90°
135°
θ
COMPUTER RESULTS FROM [5]
RICE'S APPROXIMATION [2]
NON-HARDENING LIMIT OF SINGULAR TERM FOR POWER LAW HARDENING [3, 4, 10]
PROCEDURE A
PROCEDURE B

FIG. 17

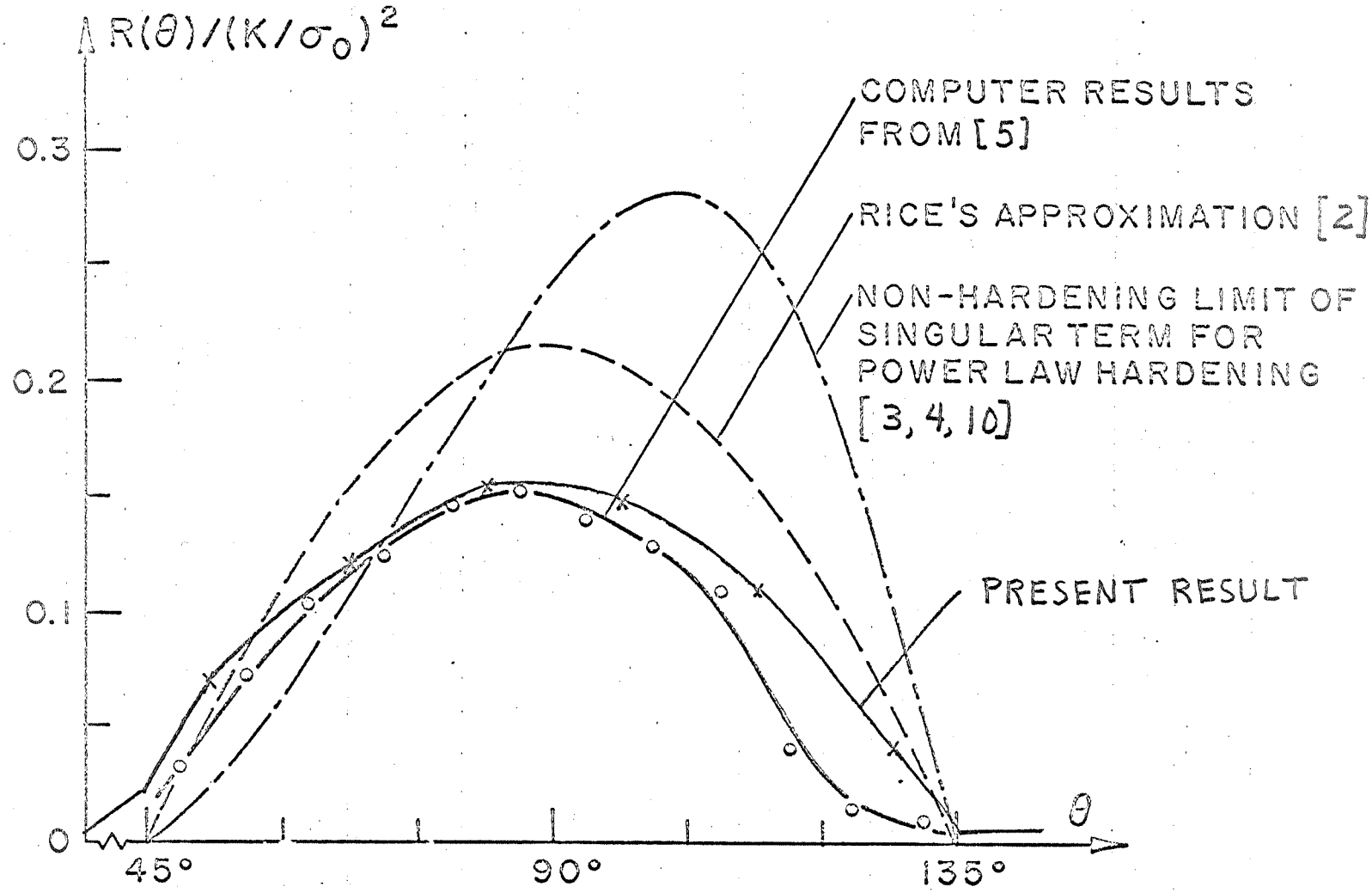
$R(\theta)/(K/\sigma_0)^2$
0.3
0.2
0.1
0
45°
90°
135°
θ
COMPUTER RESULTS FROM [5]
RICE'S APPROXIMATION [2]
NON-HARDENING LIMIT OF SINGULAR TERM FOR POWER LAW HARDENING [3, 4, 10]
PRESENT RESULT

FIG. 18a

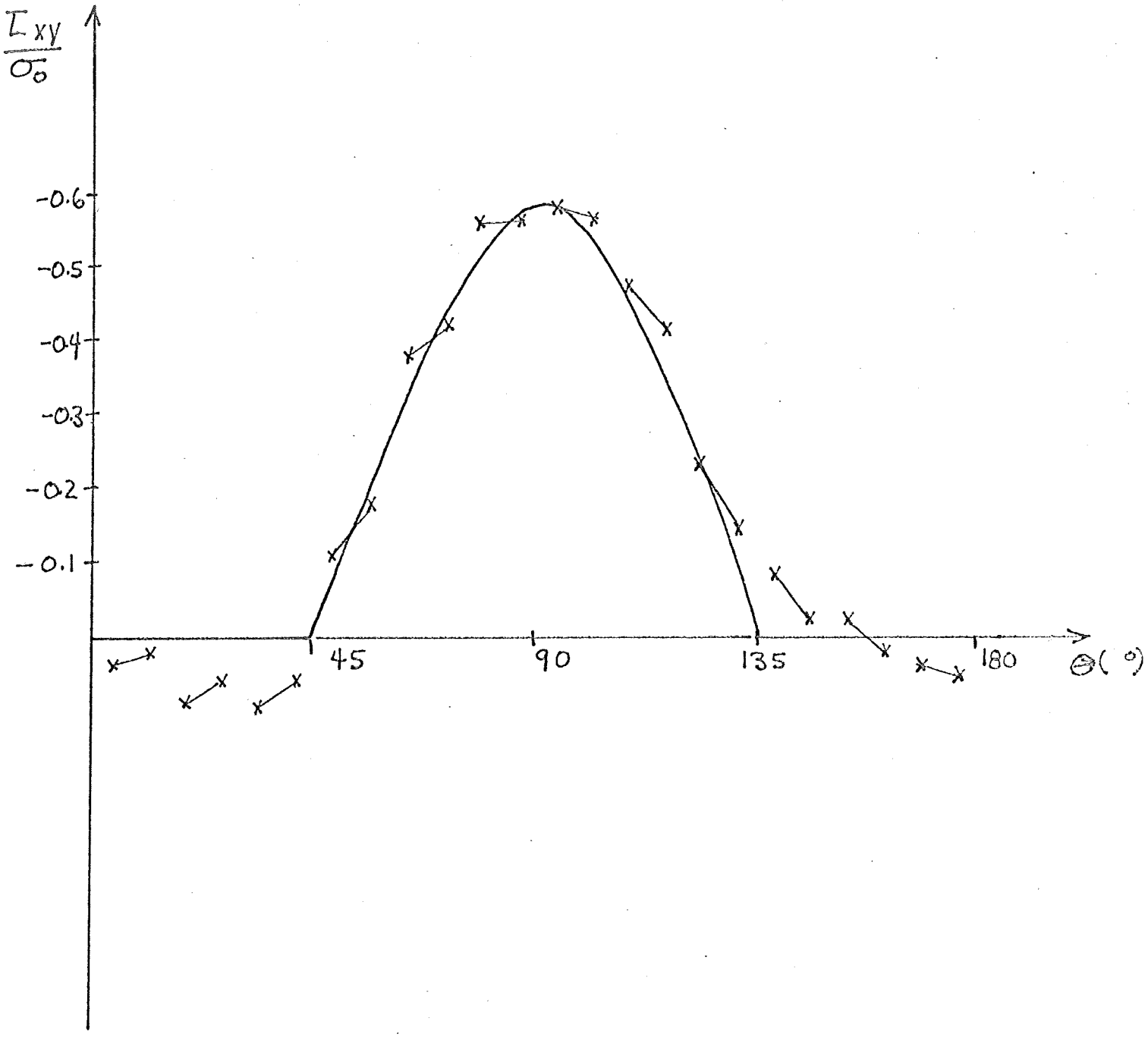

FIG. 18b

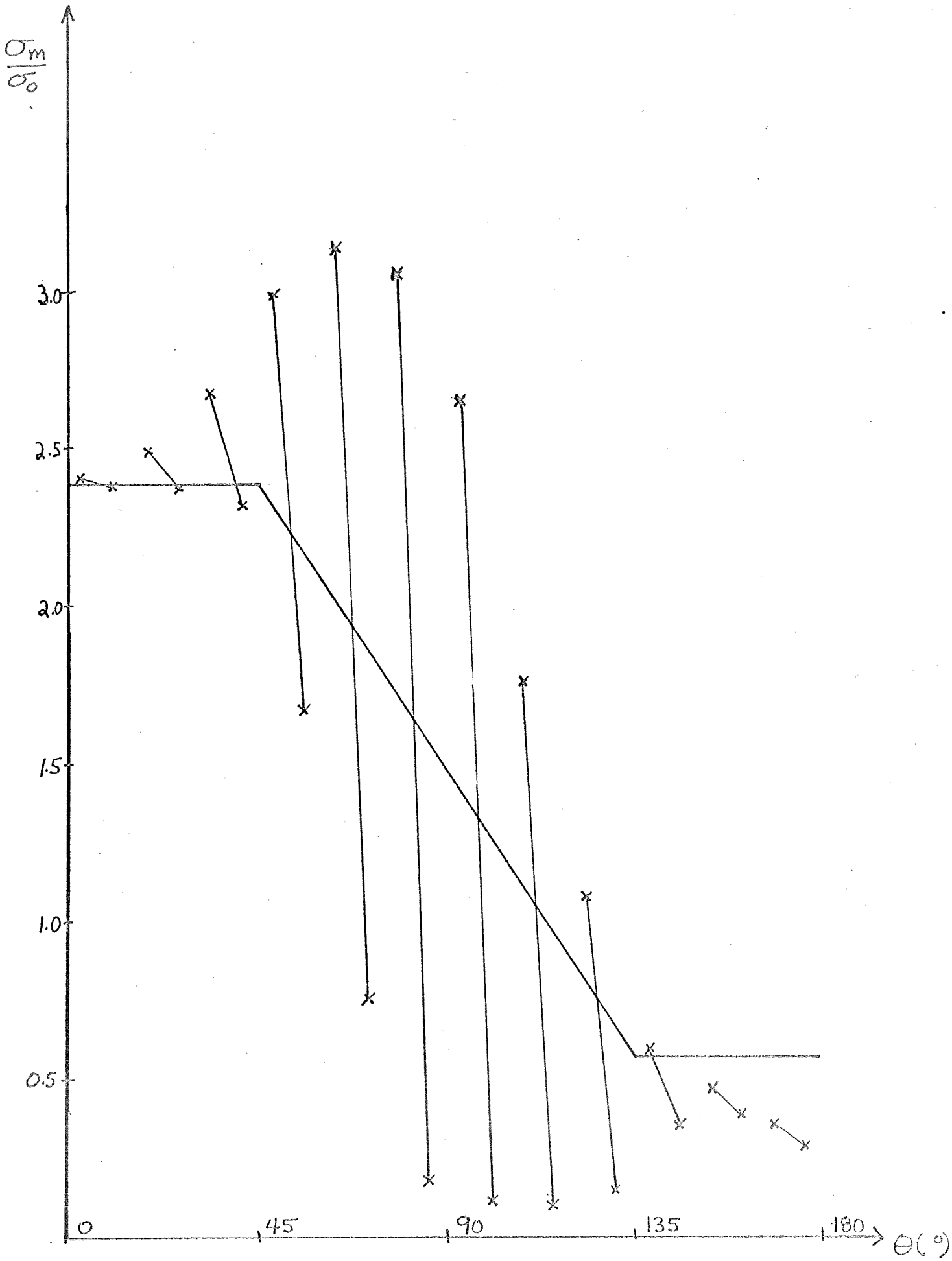

FIG. 18c

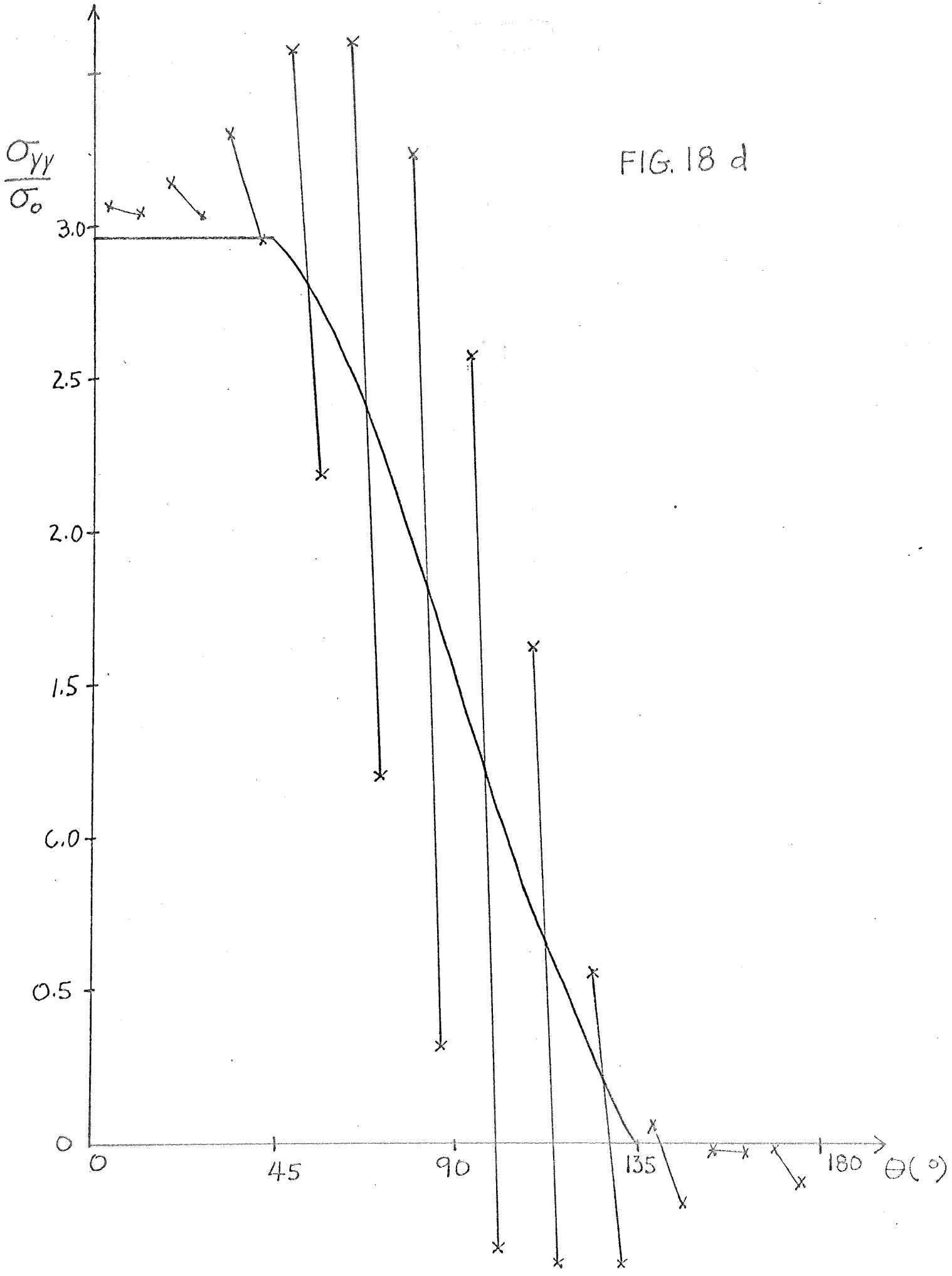

FIG. 18 d

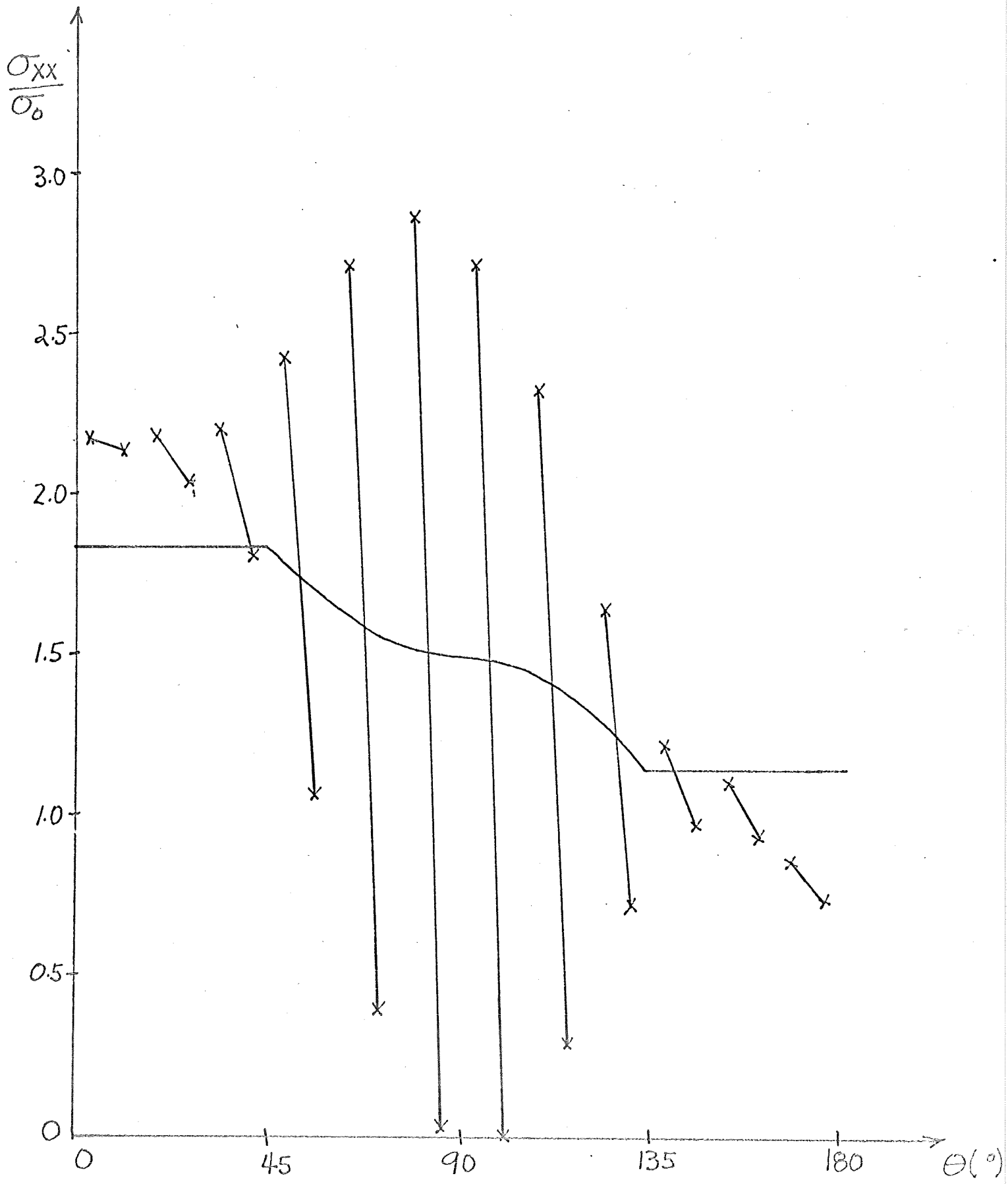

FIG. 18 e

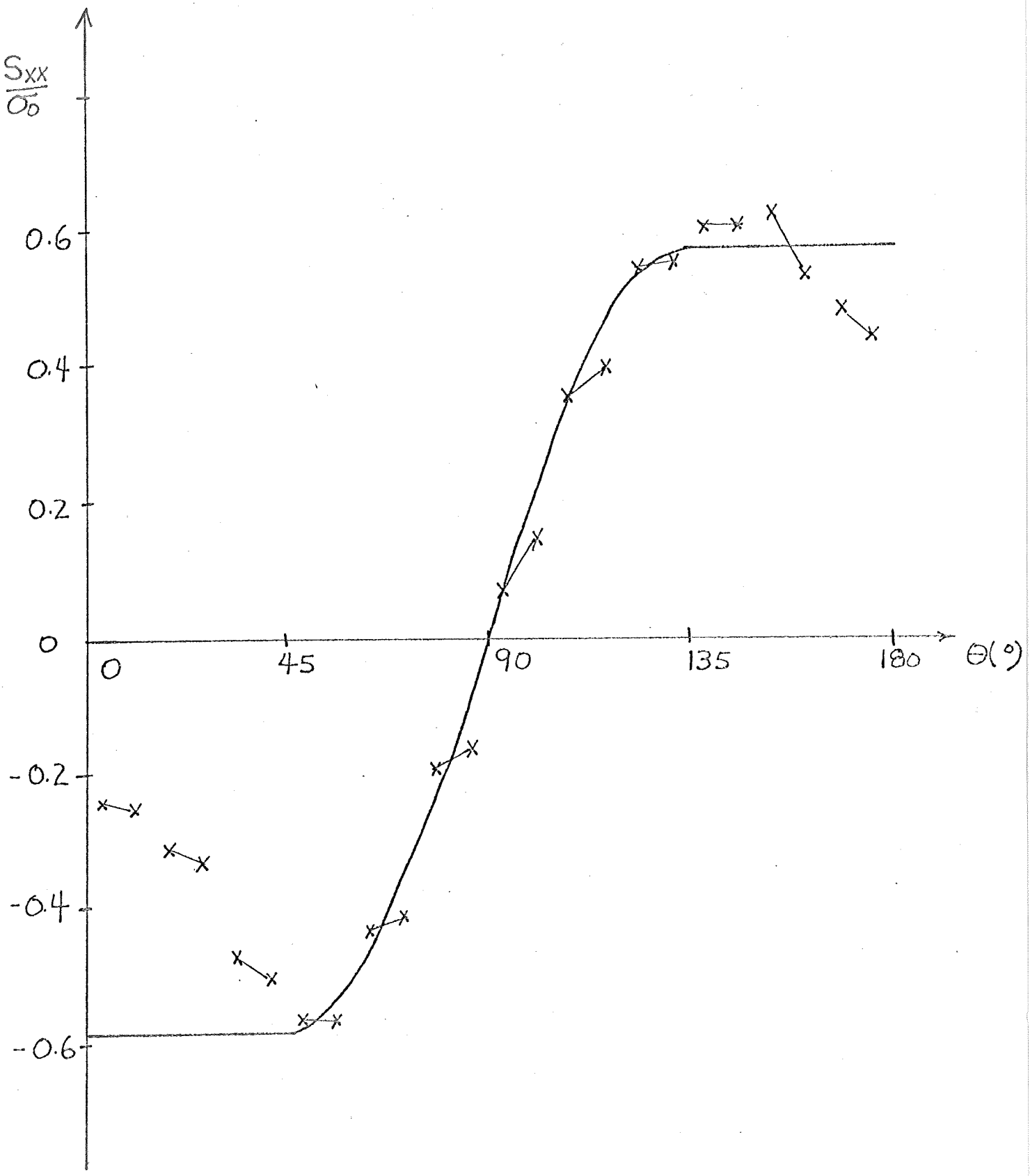

FIG. 18 f

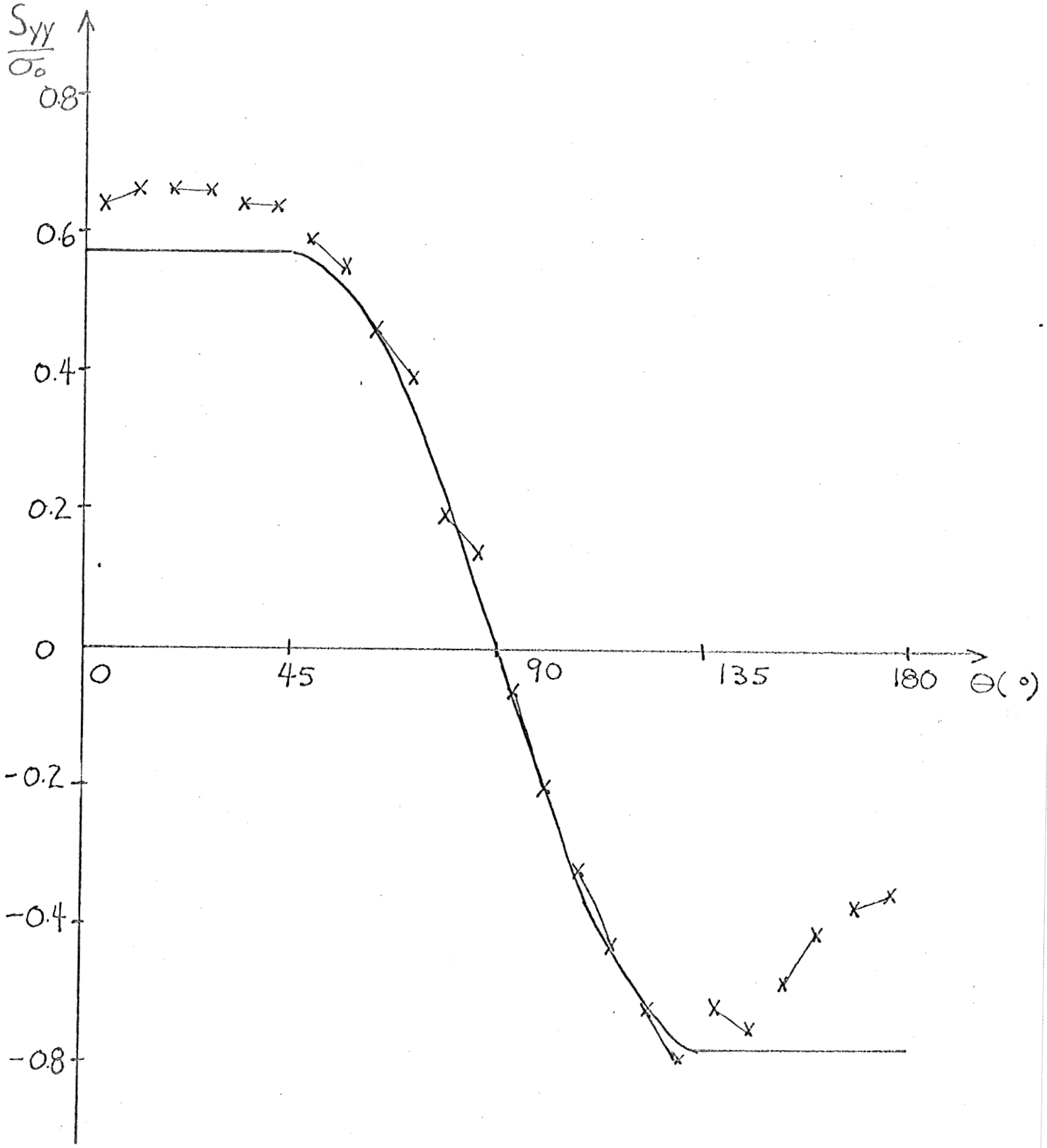

FIG. 18 g

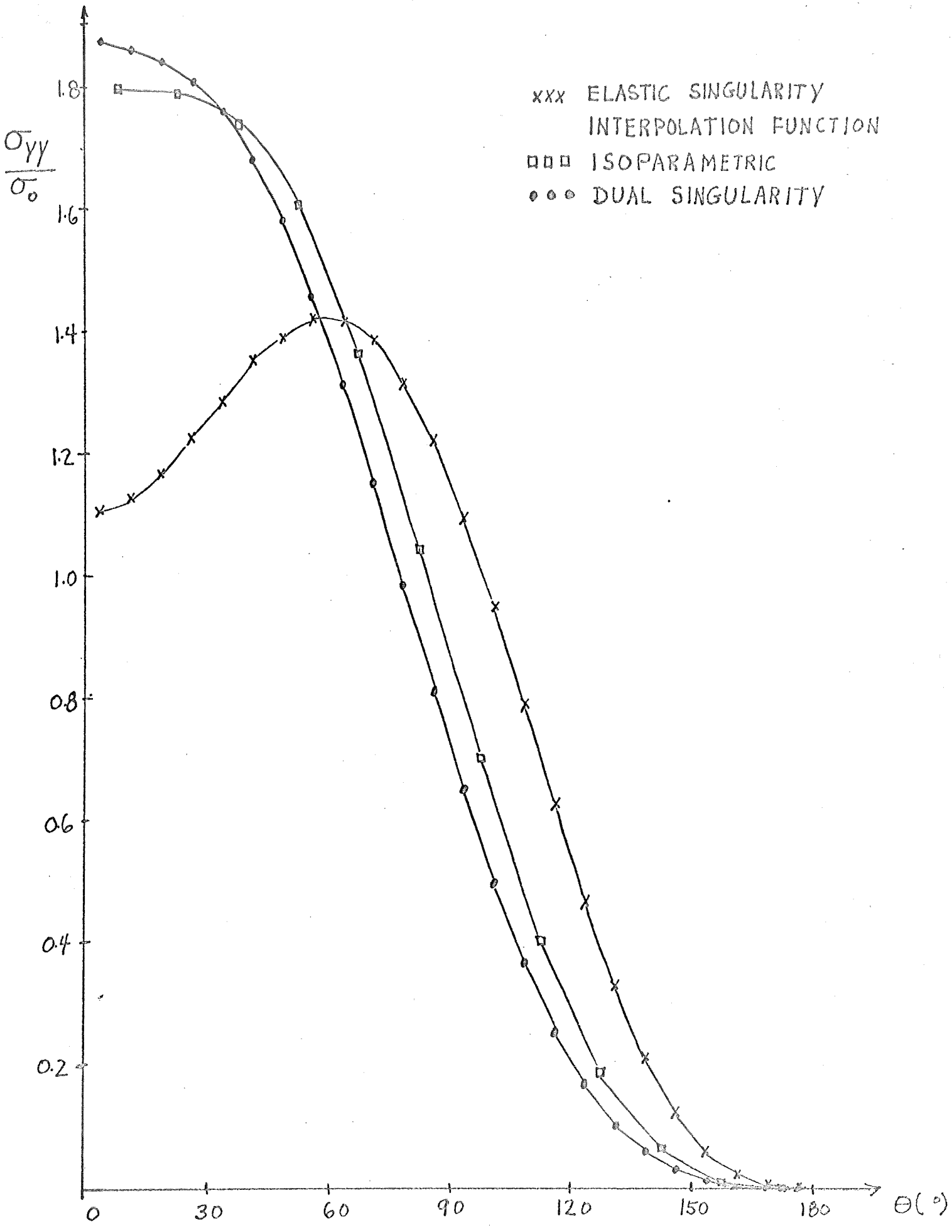
xxx ELASTIC SINGULARITY
INTERPOLATION FUNCTION
□□□ ISOPARAMETRIC
ooo DUAL SINGULARITY
$\frac{\sigma_{yy}}{\sigma_0}$
1.8
1.6
1.4
1.2
1.0
0.8
0.6
0.4
0.2
0
30
60
90
120
150
180
θ(°)

FIG. 19a

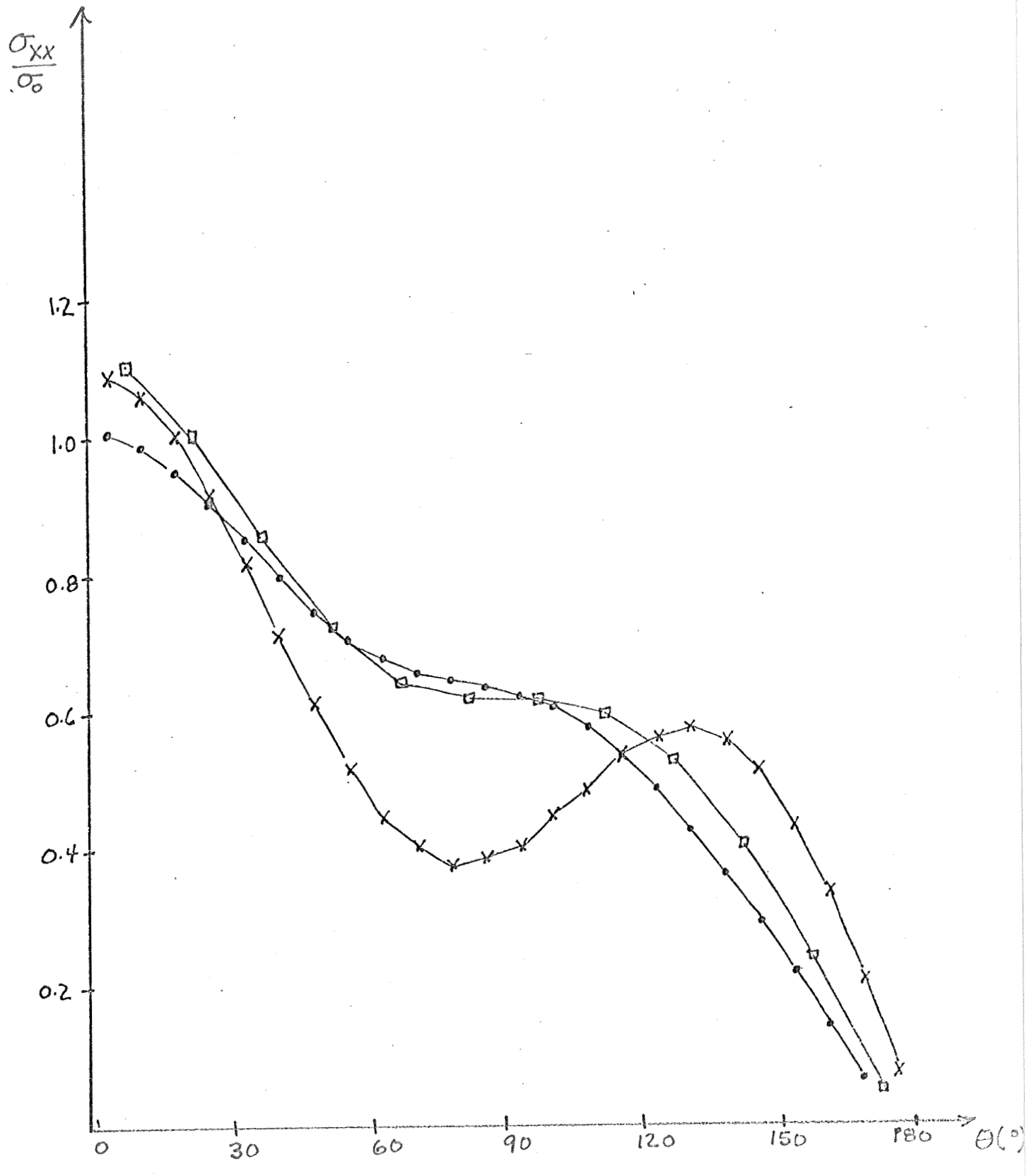

FIG. 19b

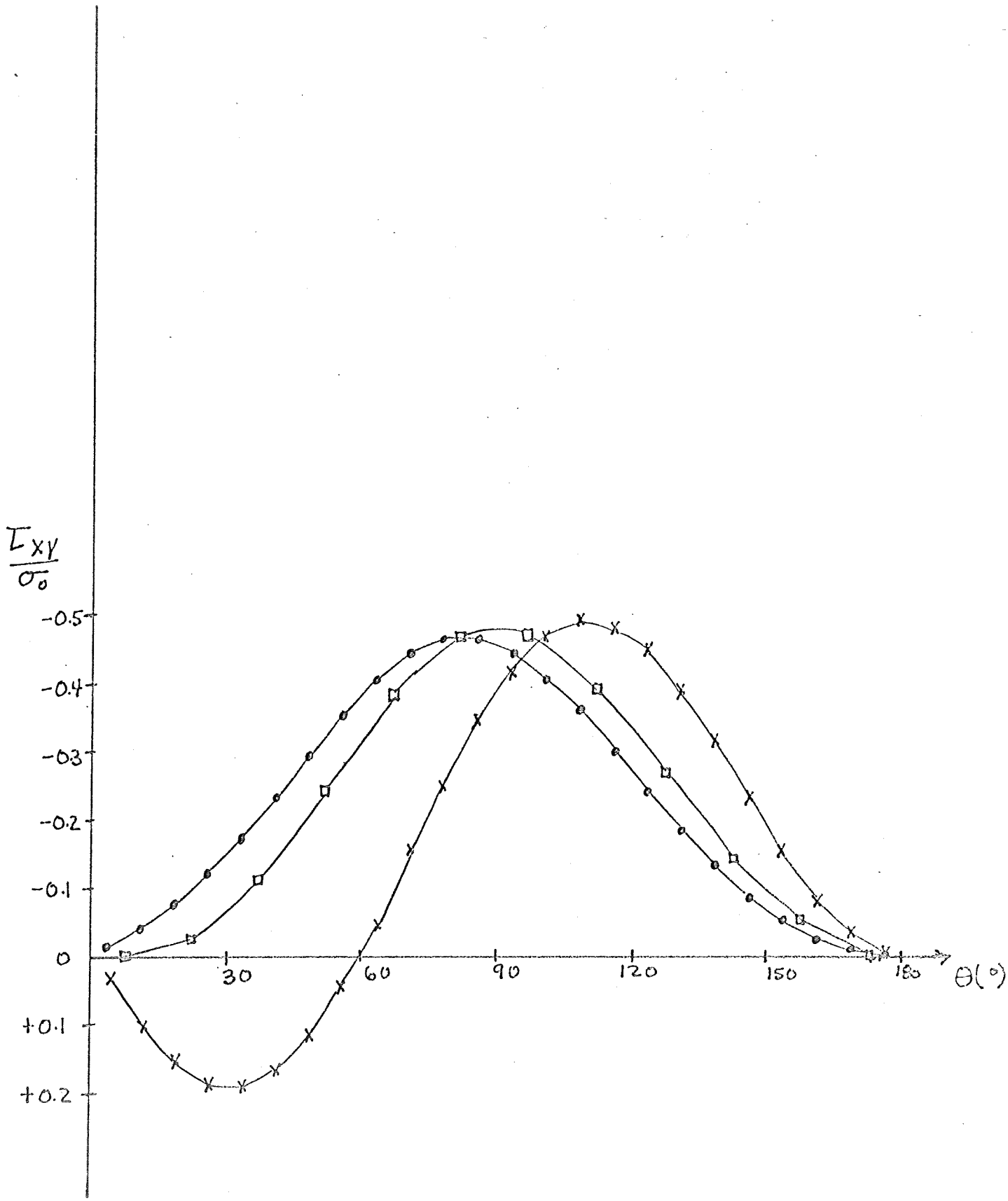

FIG. 19c

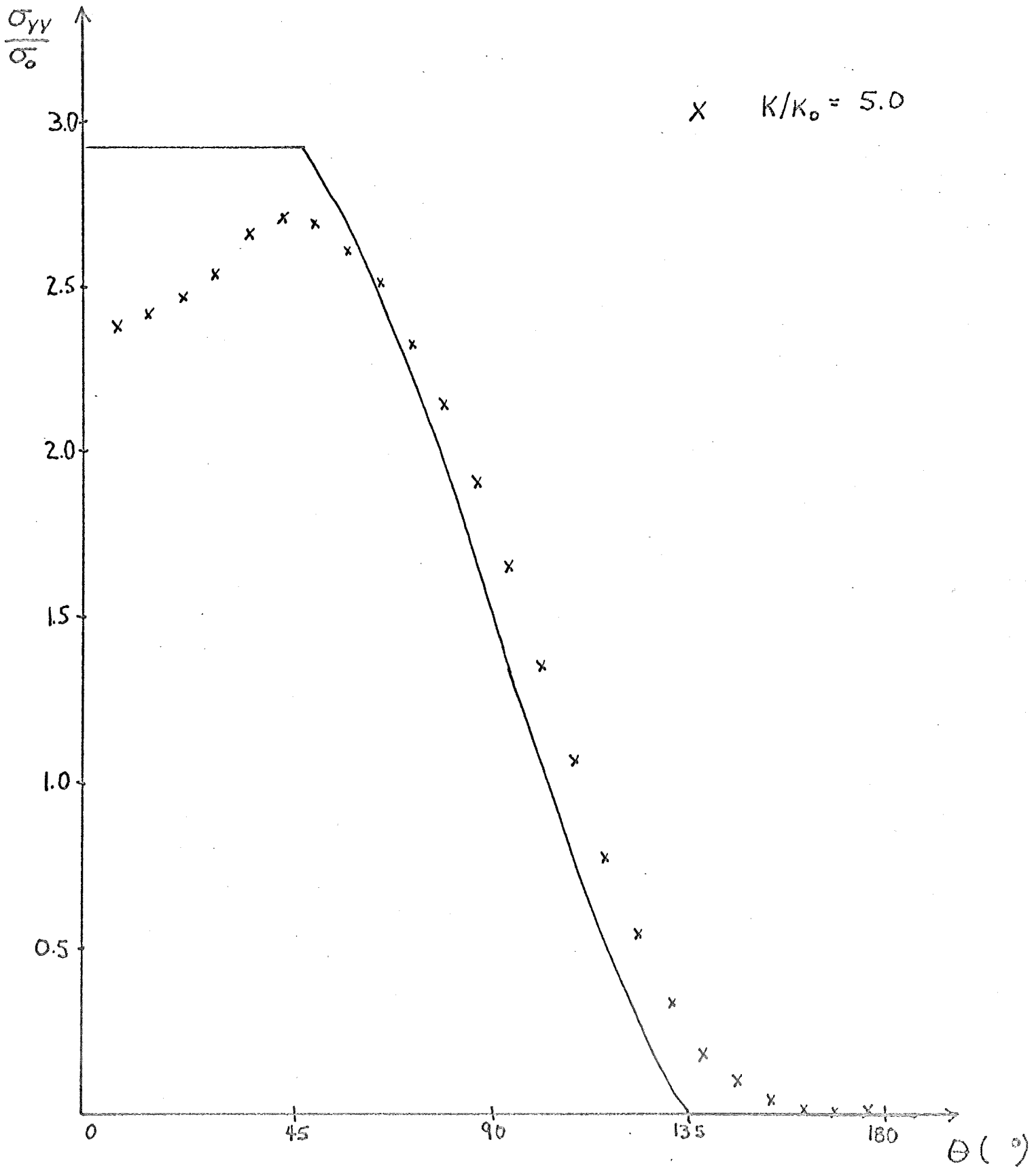

FIG. 20a

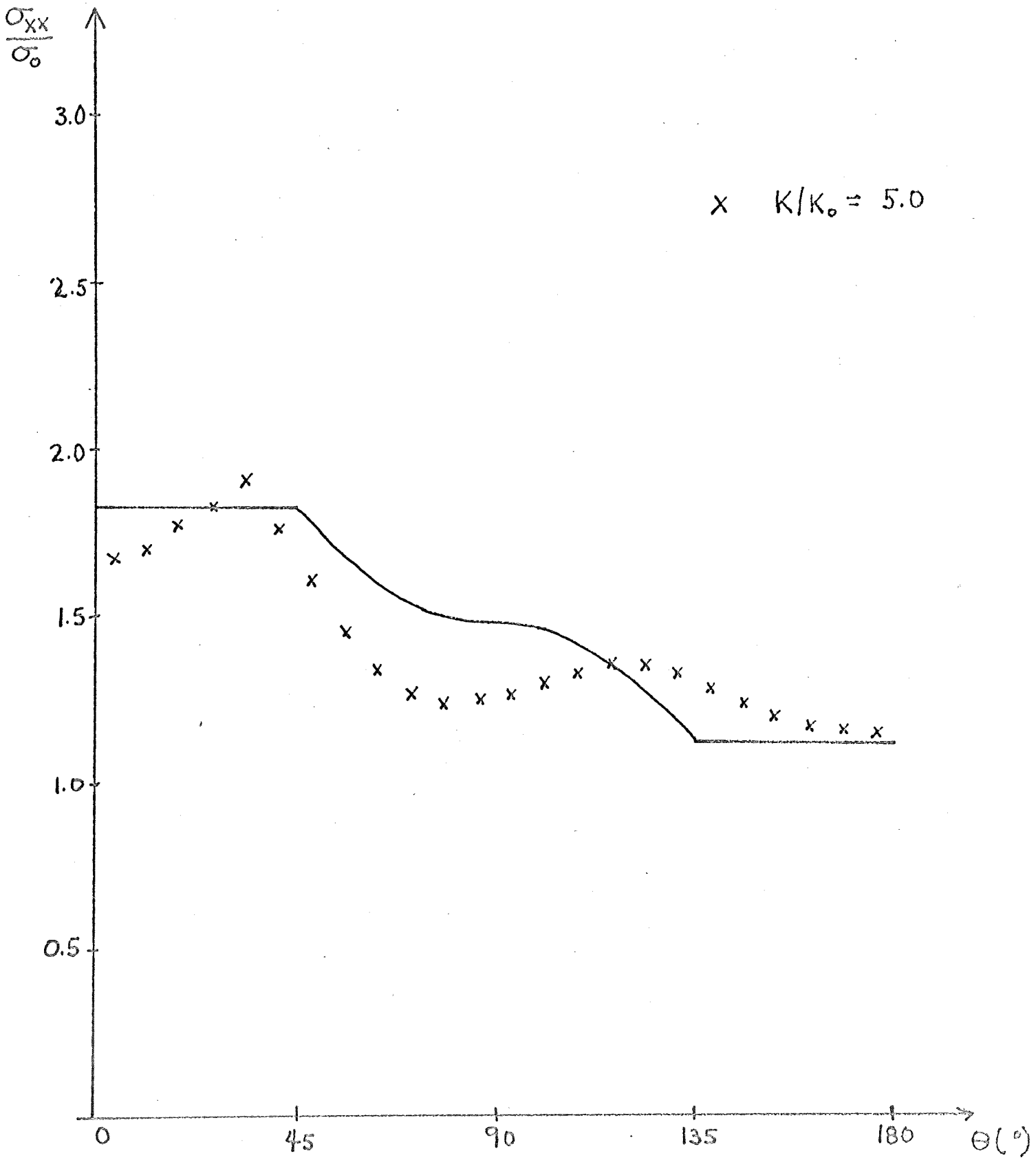

FIG. 20 b

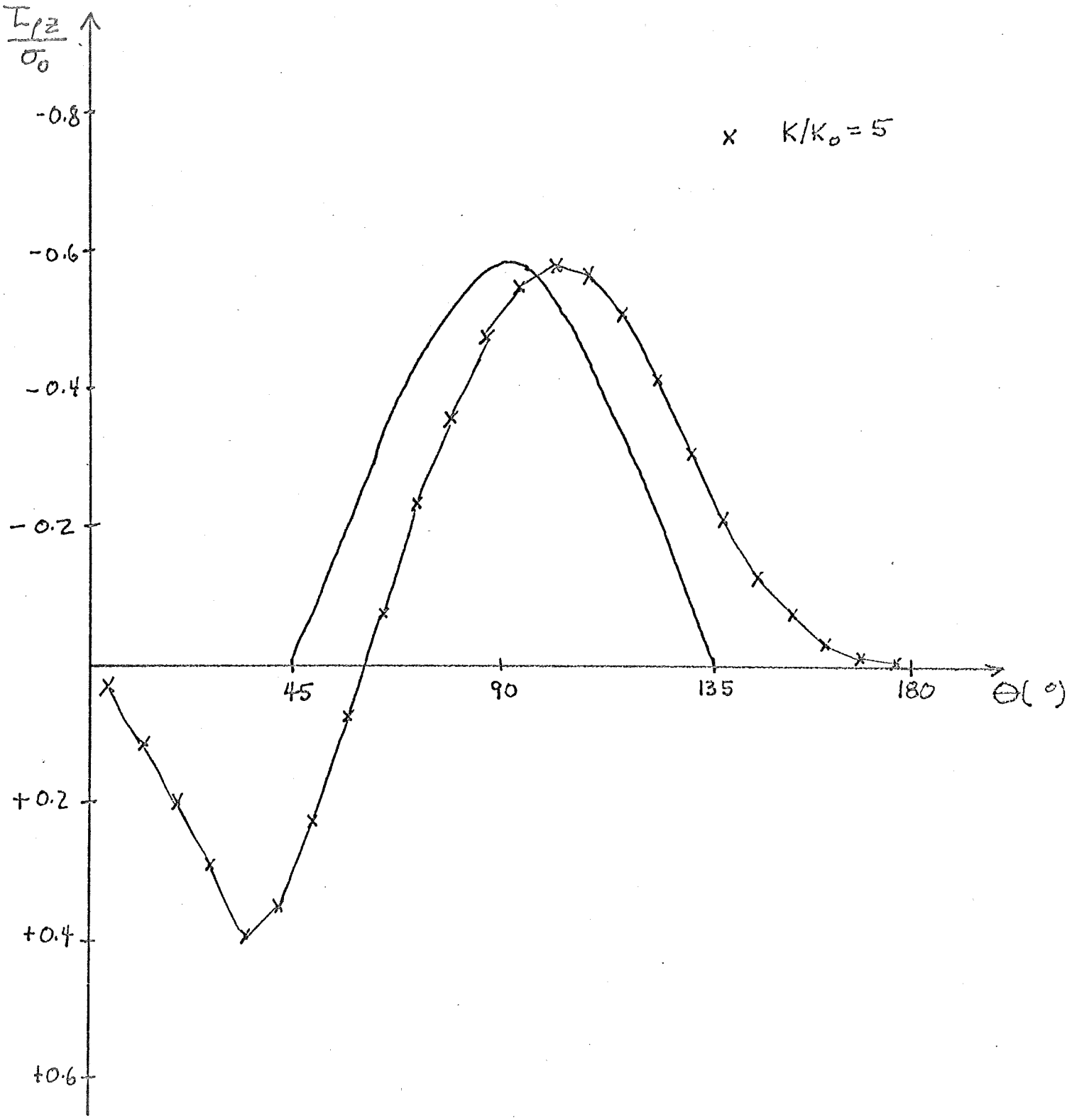

FIG. 20c

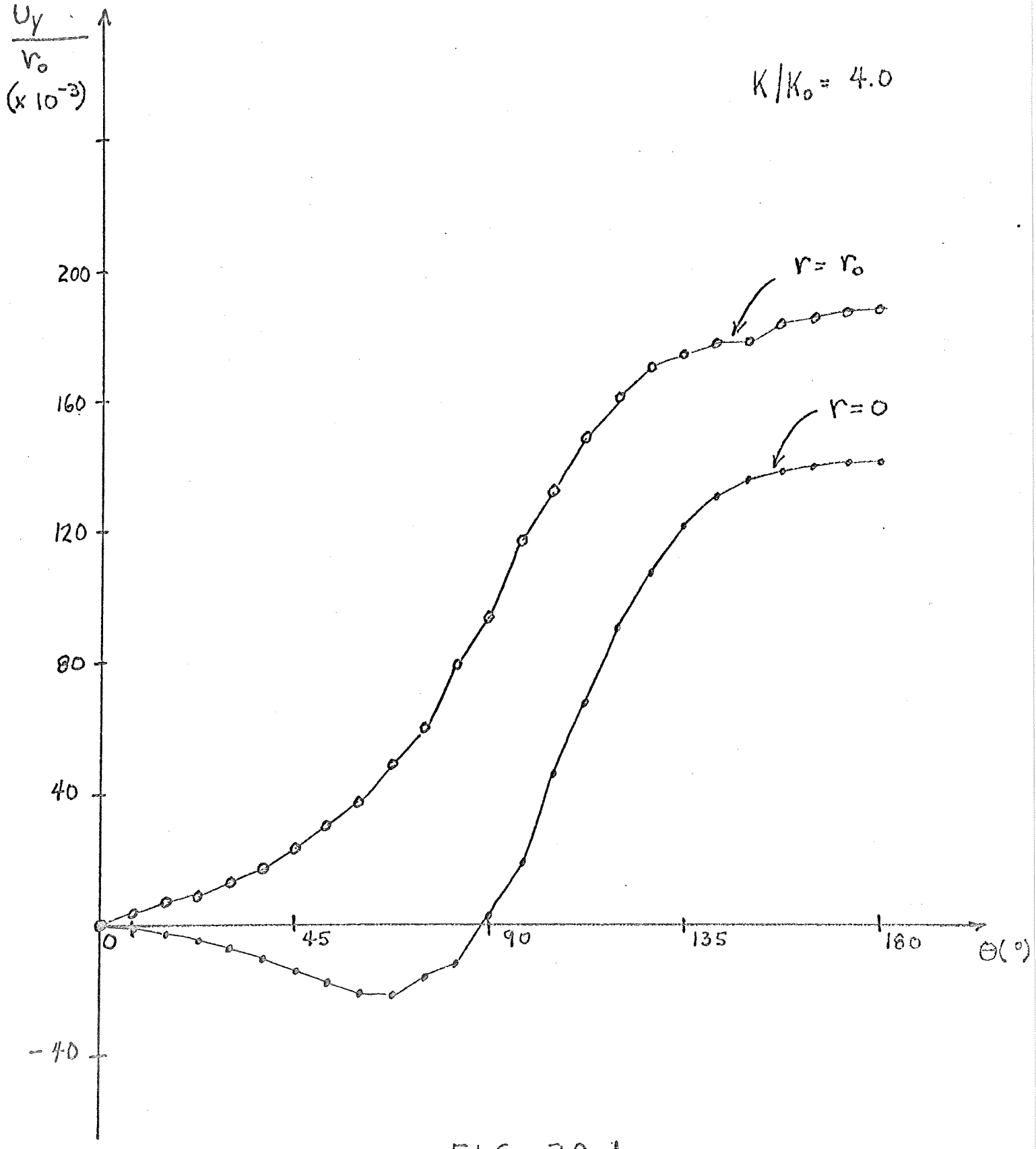
$\frac{U_y}{r_o}$
$(x\ 10^{-3})$
$K/K_o = 4.0$
200
160
120
80
40
-40
$r = r_o$
$r = 0$
0
45
90
135
180
$\Theta(^\circ)$

FIG. 20 d

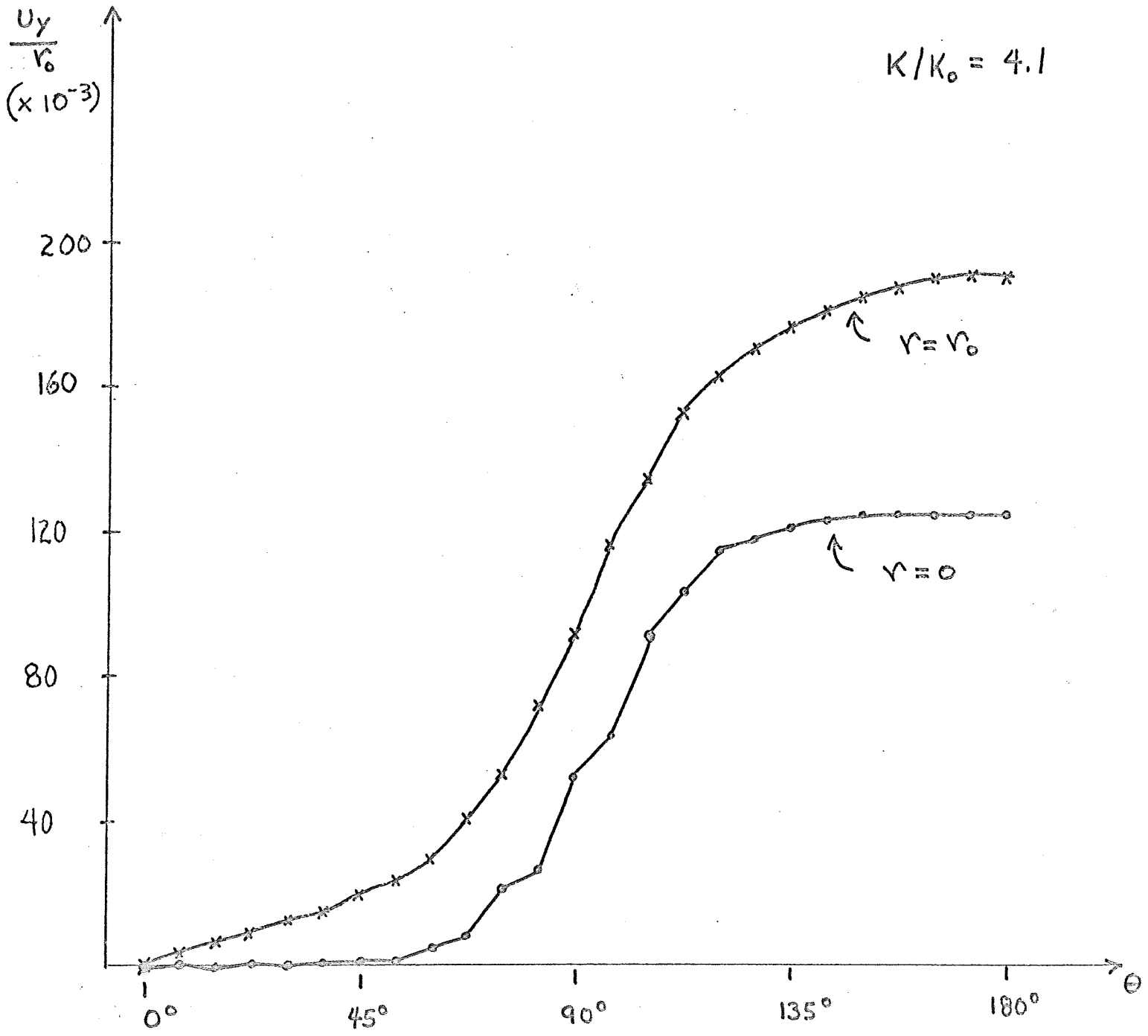

FIG. 21 a

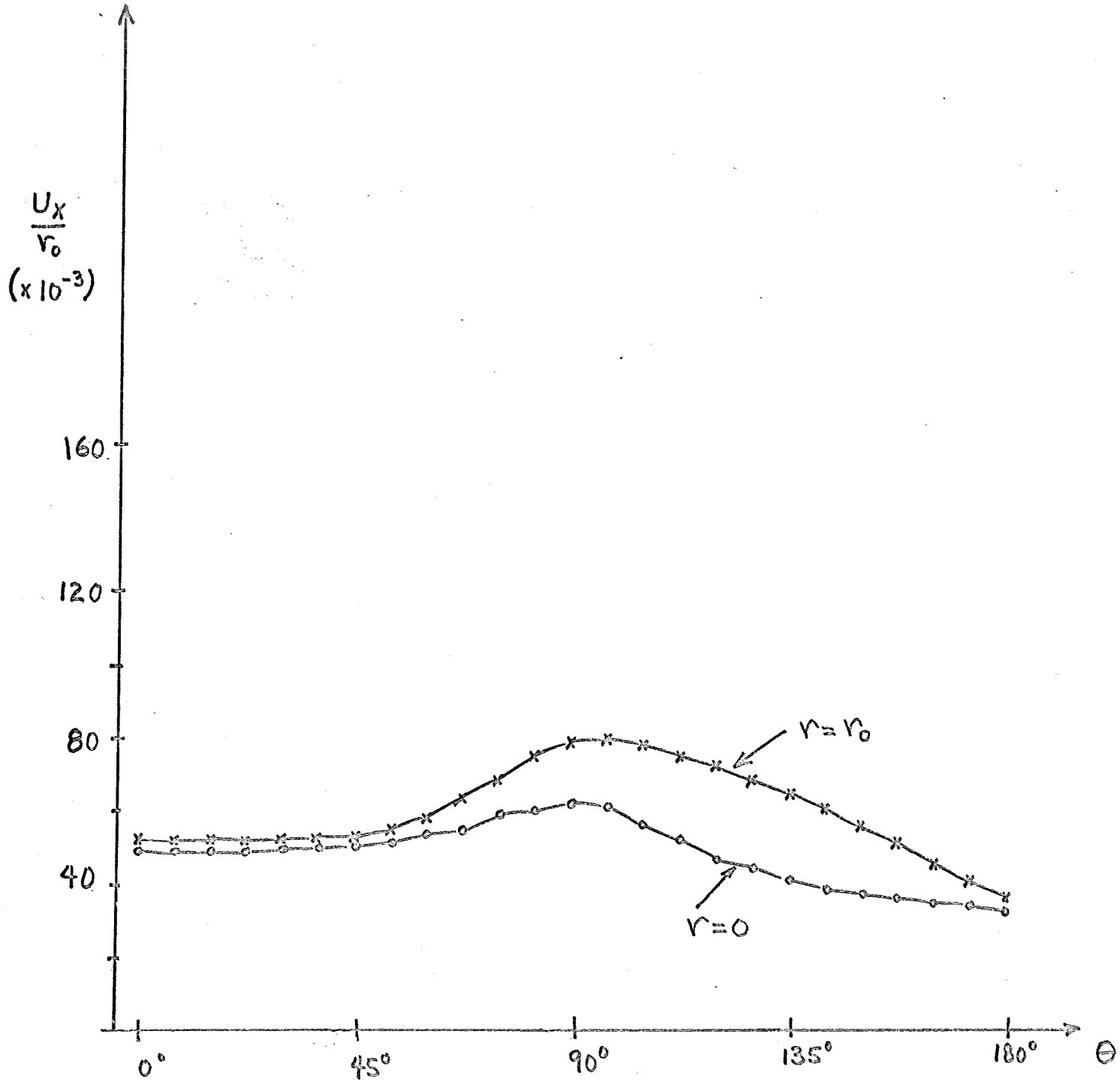

FIG. 21 b

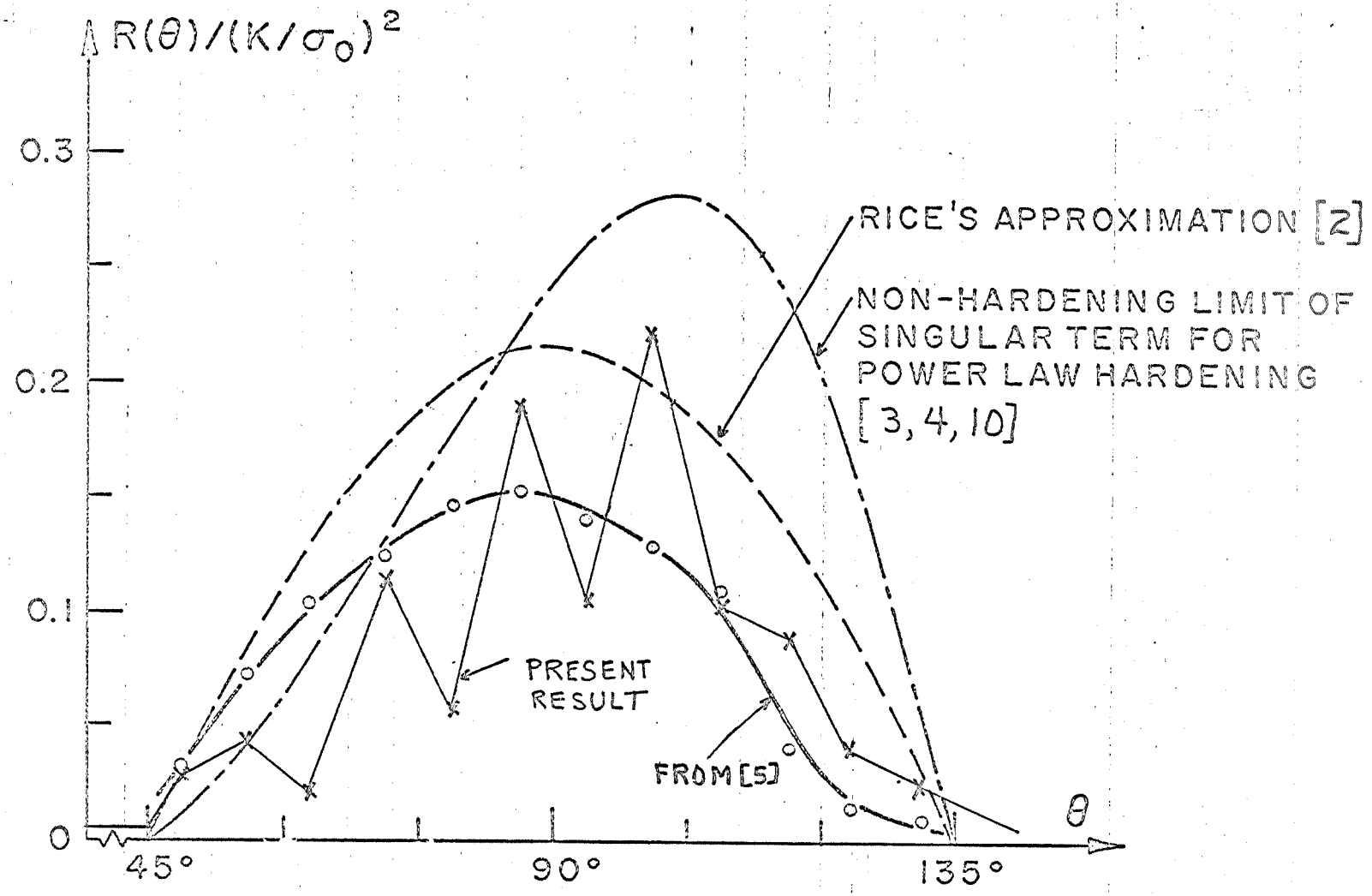
$R(\theta)/(K/\sigma_0)^2$
0.3
0.2
0.1
0
45°
90°
135°
θ
RICE'S APPROXIMATION [2]
NON-HARDENING LIMIT OF SINGULAR TERM FOR POWER LAW HARDENING [3, 4, 10]
PRESENT RESULT
FROM [5]

FIG. 21c

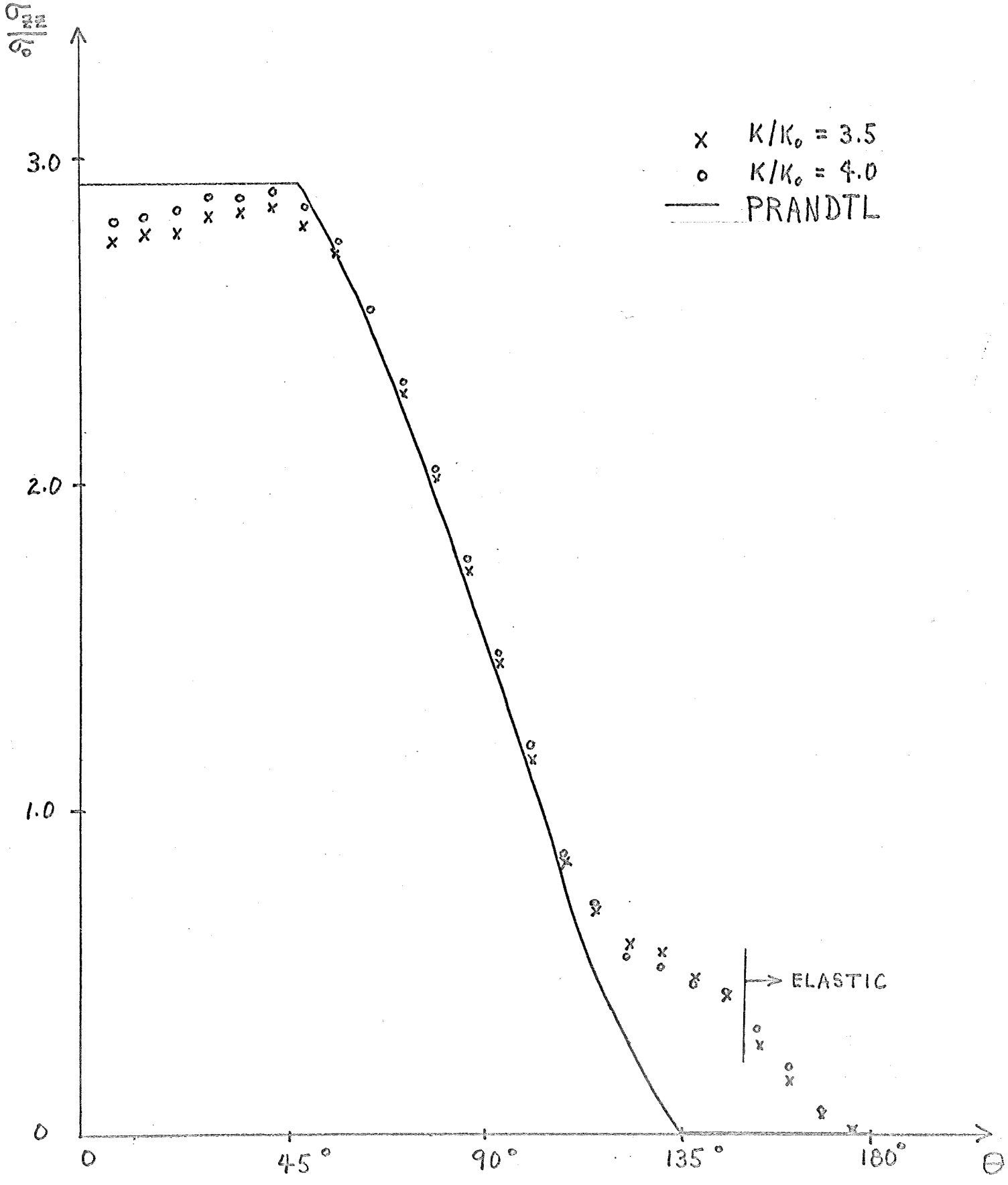
σ_{zz}/σ_o
3.0
2.0
1.0
0
0
45°
90°
135°
180°
θ
× K/K₀ = 3.5
o K/K₀ = 4.0
PRANDTL
ELASTIC

FIG. 21 d

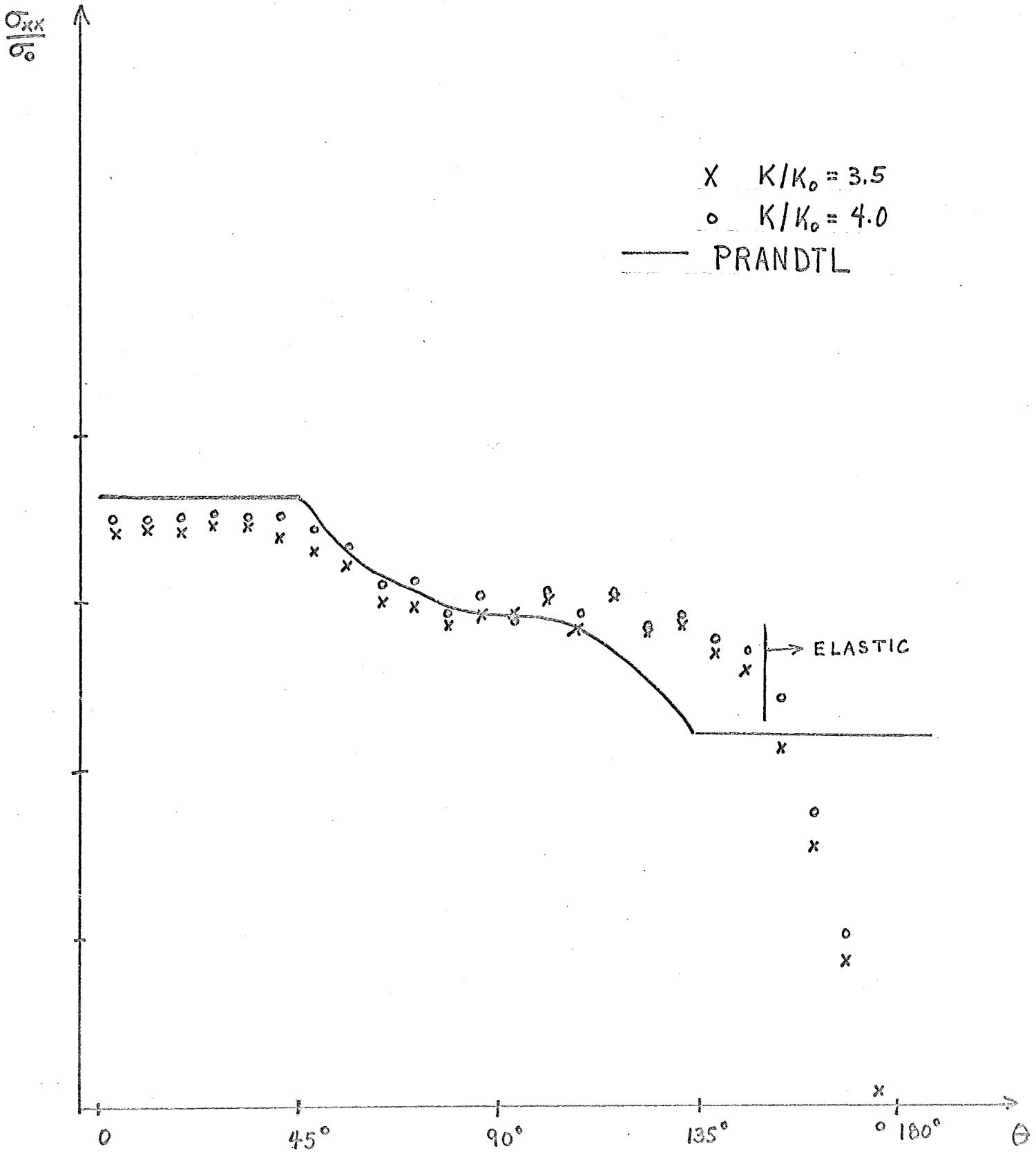
$\frac{\sigma_{xx}}{\sigma_o}$
X $K/K_o = 3.5$
o $K/K_o = 4.0$
PRANDTL
ELASTIC
0
45°
90°
135°
180°
θ

FIG. 21e

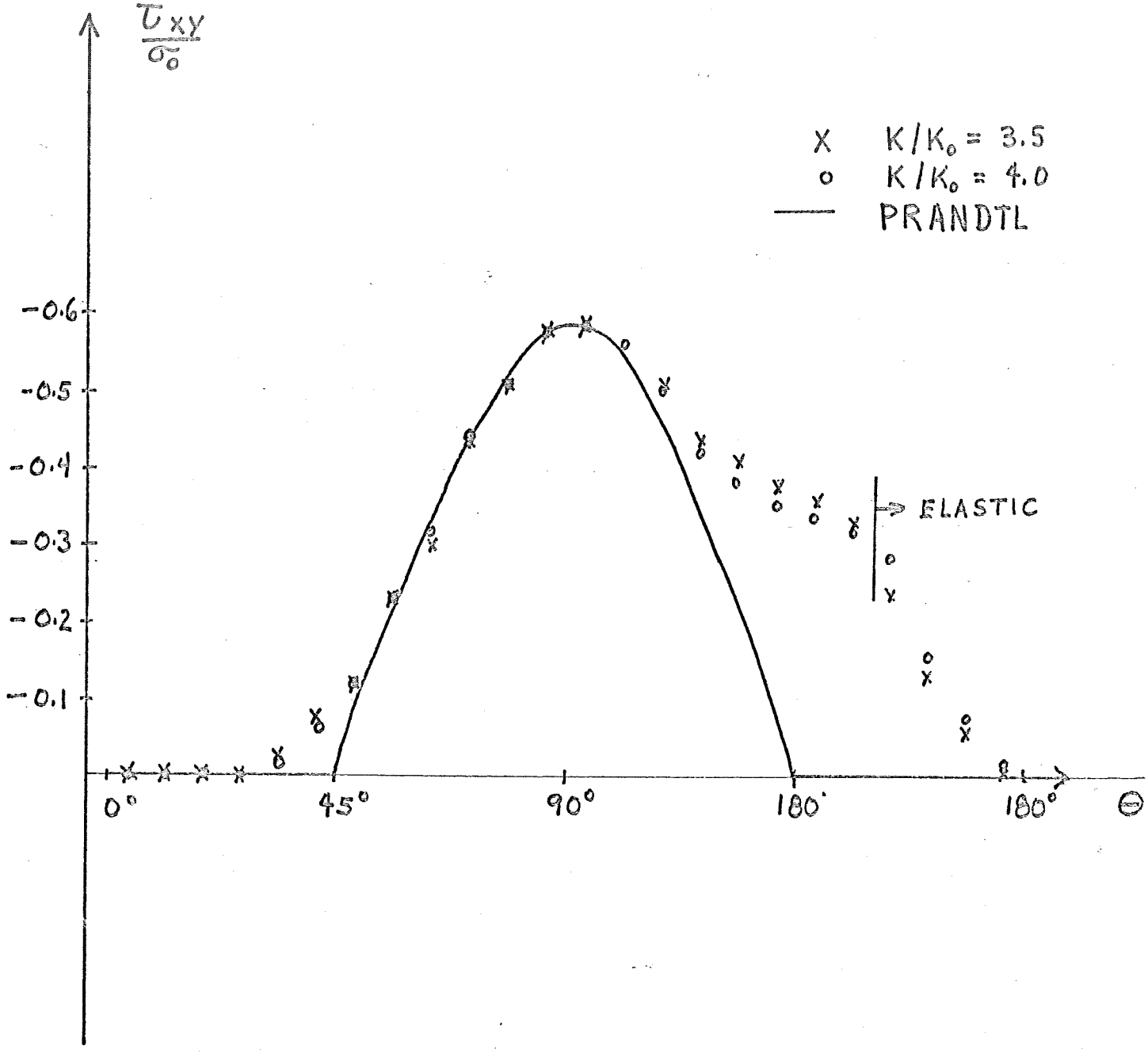
$\frac{\tau_{xy}}{\sigma_0}$
X $K/K_0 = 3.5$
o $K/K_0 = 4.0$
PRANDTL
ELASTIC
-0.6
-0.5
-0.4
-0.3
-0.2
-0.1
0°
45°
90°
180°
180°
Θ

FIG. 21 f